

Sensitivity of 24-h Forecast Dryline Position and Structure to Boundary Layer Parameterizations in Convection-Allowing WRF Model Simulations

ADAM J. CLARK,^{*,†} MICHAEL C. CONIGLIO,[†] BRICE E. COFFER,[#] GREG THOMPSON,[@]
MING XUE,^{&,*} AND FANYOU KONG^{**}

^{*} Cooperative Institute for Mesoscale Meteorological Studies, University of Oklahoma, Norman, Oklahoma

[†] NOAA/OAR/National Severe Storms Laboratory, Norman, Oklahoma

[#] Department of Marine, Earth, and Atmospheric Sciences, North Carolina State University, Raleigh, North Carolina

[@] National Center for Atmospheric Research, Boulder, Colorado

[&] School of Meteorology, University of Oklahoma, Norman, Oklahoma

^{**} Center for Analysis and Prediction of Storms, University of Oklahoma, Norman, Oklahoma

(Manuscript received 2 July 2014, in final form 11 December 2014)

ABSTRACT

Recent NOAA Hazardous Weather Testbed Spring Forecasting Experiments have emphasized the sensitivity of forecast sensible weather fields to how boundary layer processes are represented in the Weather Research and Forecasting (WRF) Model. Thus, since 2010, the Center for Analysis and Prediction of Storms has configured at least three members of their WRF-based Storm-Scale Ensemble Forecast (SSEF) system specifically for examination of sensitivities to parameterizations of turbulent mixing, including the Mellor–Yamada–Janjić (MYJ); quasi-normal scale elimination (QNSE); Asymmetrical Convective Model, version 2 (ACM2); Yonsei University (YSU); and Mellor–Yamada–Nakanishi–Niino (MYNN) schemes (hereafter PBL members). In postexperiment analyses, significant differences in forecast boundary layer structure and evolution have been observed, and for preconvective environments MYNN was found to have a superior depiction of temperature and moisture profiles. This study evaluates the 24-h forecast dryline positions in the SSEF system PBL members during the period April–June 2010–12 and documents sensitivities of the vertical distribution of thermodynamic and kinematic variables in near-dryline environments. Main results include the following. Despite having superior temperature and moisture profiles, as indicated by a previous study, MYNN was one of the worst-performing PBL members, exhibiting large eastward errors in forecast dryline position. During April–June 2010–11, a dry bias in the North American Mesoscale Forecast System (NAM) initial conditions largely contributed to eastward dryline errors in all PBL members. An upgrade to the NAM and assimilation system in October 2011 apparently fixed the dry bias, reducing eastward errors. Large sensitivities of CAPE and low-level shear to the PBL schemes were found, which were largest between 1.0° and 3.0° to the east of drylines. Finally, modifications to YSU to decrease vertical mixing and mitigate its warm and dry bias greatly reduced eastward dryline errors.

1. Introduction

One of the biggest challenges facing the current generation of high-resolution numerical weather prediction models is accurately forecasting the structure and evolution of the planetary boundary layer (PBL), which has direct impacts on forecasting sensible weather like low-level temperature, moisture, and winds, as well as

instability and convective initiation (e.g., Marshall et al. 2003; Roebber et al. 2004; Hu et al. 2010; Coniglio et al. 2013). Because current models are still too coarse to resolve even the largest turbulent eddies that vertically transport heat, moisture, and momentum in the PBL, these transport processes must be parameterized, which can quickly introduce large forecast errors.

These PBL forecast uncertainties motivated a major emphasis of recent NOAA/Hazardous Weather Testbed Spring Forecasting Experiments (SFEs; e.g., Clark et al. 2012), which involves examining low-level thermodynamic and kinematic fields in Weather Research and Forecasting (WRF; Skamarock et al. 2008) Model

Corresponding author address: Adam J. Clark, National Weather Center, NSSL/FRDD, 120 David L. Boren Blvd., Norman, OK 73072.

E-mail: adam.clark@noaa.gov

simulations identically configured except for their scheme to parameterize vertical effects of turbulent mixing.¹ In fact, each year since 2010, the Center for Analysis and Prediction of Storms (CAPS) has configured at least three members of their 4-km grid spacing Storm-Scale Ensemble Forecast (SSEF) system specifically for examination of sensitivities to PBL schemes, including the Mellor–Yamada–Janjić (MYJ; Mellor and Yamada 1982; Janjić 2002); quasi-normal scale elimination (QNSE; Sukoriansky et al. 2005); Asymmetrical Convective Model, version 2 (ACM2; Pleim 2007); Yonsei University (YSU; Noh et al. 2003); and Mellor–Yamada–Nakanishi–Niino (MYNN; Nakanishi 2000, 2001; Nakanishi and Niino 2004, 2006) schemes. The MYNN, MYJ, and QNSE schemes are considered “local” because they use model fields only at adjacent levels to determine the turbulent fluxes. The ACM2 and YSU schemes are considered “nonlocal” because they use model fields at a range of levels to simulate the effect of large eddies in the convective PBL. Coniglio et al. (2013) provide additional details regarding the formulations of these schemes.

To date, the most thorough objective examination of PBL schemes used for SFEs was presented in Coniglio et al. (2013), in which forecast thermodynamic variables were evaluated using radiosonde observations upstream from deep convection. For forecasts valid during the evening, Coniglio et al. (2013) found that the local MYJ and QNSE schemes produce PBLs that are generally too shallow and moist while the nonlocal ACM2 and YSU schemes produce PBLs that are too deep and dry. The best results were found for MYNN, which was nearly unbiased in PBL depth, moisture, and potential temperature, with forecasts comparable to those from the operational North American Mesoscale Forecast System (NAM; Rogers et al. 2009). Coniglio et al. (2013) conclude that these results give confidence in the use of MYNN over MYJ in preconvective environments in convection-allowing WRF Model configurations. Similar positive results for MYNN have led model developers working on the High Resolution Rapid Refresh (HRRR; Alexander et al. 2013) model to switch from using the MYJ to the MYNN scheme. Hu et al. (2010) find similar results to Coniglio et al. (2013), but only when examining the YSU, ACM2, and MYJ schemes.

Although MYNN has performed well in recent comparison studies, Coniglio et al. (2013) stress that this superior performance should not necessarily translate

into better forecasts of convection or other aspects of simulations impacted by turbulent mixing like the positioning of drylines and fronts. Thus, to build on the work of Coniglio et al. (2013), this study examines the same set of simulations, but the PBL schemes are evaluated according to forecast dryline position. Additionally, thermodynamic and kinematic variables associated with the dryline and near-dryline environments are examined, which includes examination of dryline-relative composite vertical cross sections, soundings, and the dryline-induced vertical circulations. Drylines are important because of their frequent role in convective initiation over the southern high plains (e.g., Fujita 1958; Rhea 1966; Schaefer 1986). Furthermore, knowledge of precise dryline position when present along with other environmental factors important for severe weather (i.e., instability and vertical wind shear) is crucial for accurately delineating severe weather risk areas by forecasters at agencies such as the Storm Prediction Center (SPC). Finally, evaluating forecast dryline positions for different PBL schemes is also strongly motivated by Coffey et al. (2013), who examined 24-h forecast dryline position errors in a 4-km grid spacing version of the WRF Model run daily at the National Severe Storms Laboratory (NSSL), known as the NSSL-WRF. Examining 116 dryline cases over a 5-yr period, Coffey et al. (2013) found that the NSSL-WRF, which uses the MYJ scheme, had a systematic eastward bias of about 0.5°, which was present across a wide spectrum of dryline cases. Thus, herein, we are particularly interested in whether the WRF Model simulations conducted by CAPS for the 2010–12 SFEs exhibit this eastward bias and whether MYNN, which performed best in the Coniglio et al. (2013) evaluations, also exhibits superior performance in forecasting dryline position. The remainder of the study is organized as follows. Section 2 presents information on WRF Model configurations, analysis datasets, and dryline identification methods. Section 3 presents results, which includes two case studies and aggregated statistics over various sets of cases. Section 4 provides a summary and conclusions.

2. Data and methodology

a. WRF Model configurations and analysis dataset

Since 2007, CAPS has produced various versions of its SSEF system in support of annual NOAA/Hazardous Weather Testbed SFEs (e.g., Xue et al. 2010; Kong et al. 2010, 2011). The basic strategy in configuring the ensemble is to have one subset of members accounting for as many error sources as possible to be used for ensemble forecasting, and another set of members configured for examination of physics sensitivities, which has mainly

¹ Although these schemes act at all model levels, they are commonly referred to as PBL schemes because most of the vertical mixing occurs within and near the PBL.

TABLE 1. A summary of code changes and their intended effects in YSU-T.

Description of code change	Intended effect
Surface-based convective perturbation velocity set to zero	Lower the diagnosed PBL height
When calculating the wind shear squared term in the bulk Richardson number Ri, do not assume zero wind at lower boundary but rather 25% of lowest model-level wind	Reduce downward momentum flux as a result of the large denominator in Ri from higher wind speeds close to the surface
Calculate the thermodynamic term of Ri using $\partial\theta_{IL}/\partial z$ not $\partial\theta_v/\partial z$, where θ_{IL} is ice-liquid water potential temperature and θ_v is virtual potential temperature	Treat cloud-topped boundary layers as entirely connected within the PBL; otherwise, cloud-topped PBLs result in the cloud layer being split as a fraction within and a fraction above the PBL, giving inconsistent profiles of the final mixing coefficients
Disable the explicit entrainment factor at top of the PBL	Mitigate perceived bias of excessive loss of water vapor from PBL and into the free troposphere above
Compute local Ri-based mixing coefficients as done for layers above the PBL top and assign final value as the max of the local and nonlocal values	As an offset to disabling the explicit entrainment at the top of the PBL, well-mixed PBLs topped with clouds will have higher entrainment at cloud top than without this modification

involved the examination of microphysics and PBL schemes. Herein, forecasts from the 2010–12 SFEs are examined. The 2010, 2011, and 2012 SFEs were conducted from 17 May to 18 June, 9 May to 10 June, and 7 May to 8 June, respectively, with SSEF system forecasts becoming available about 2 weeks before the start dates of each year. The subsets of SSEF system members used in this study are configured identically, except for their PBL schemes (hereafter PBL members). In two case study analyses, results from SSEF members with perturbed initial conditions (ICs) and lateral boundary conditions (LBCs) along with mixed physics are also shown.

During 2010, there were three PBL members that used the MYJ, MYNN, and QNSE schemes. During 2011, six PBL members were run that included the PBL members from 2010, as well as ACM2, YSU, and another experimental version of YSU provided by G. Thompson of NCAR (hereafter the modified YSU is referred to as YSU-T). Previous subjective evaluations of numerous model simulations using YSU by SFE participants found a dry and warm bias in the PBL in

typical late spring convective cases in the midcontinental United States that included drylines forecast too far east. These features had been noted during prototype real-time summer forecast experiments for a number of prior years. Therefore, some attempt to combat these perceived biases was attempted, which included the set of code changes summarized in Table 1.

Finally, during 2012, there were five PBL members, which consisted of the same PBL members from 2011, except for the YSU-T member. Other than the WRF Model version (3.1.1, 3.2.1, and 3.3.1 for 2010, 2011, and 2012, respectively), all other aspects of the model configurations, which are summarized in Table 2, were the same for all three of the years examined. To our knowledge, there are no major changes between the model versions that would have a significant effect on our results.

The WRF Model forecasts used 4-km grid spacing with 51 vertical levels and were initialized on weekdays at 0000 UTC and integrated for 30 or 36 h over a continental United States (CONUS) domain during the

TABLE 2. Model specifications for SSEF members with different PBL schemes. All simulations used Thompson et al. (2004) microphysics, Rapid Radiative Transfer Model (RRTM; Mlawer et al. 1997) shortwave radiation and Goddard (Chou and Suarez 1994) longwave radiation parameterizations, and the Noah (Chen and Dudhia 2001) land surface model. ARPS_a refers to ARPS 3DVAR and cloud analysis, which uses NAM analyses as the background. NAM_f refers to NAM forecasts (12-km grid spacing).

Boundary layer scheme	Years available		No. of cases		
MYJ	2010–12		40		
MYNN	2010–12		40		
QNSE	2010–12		40		
ACM2	2011–12		30		
YSU	2011–12		30		
YSU-T	2011		14		
Other model specifications (valid for all simulations)					
Microphysics	Shortwave radiation scheme	Longwave radiation scheme	Initial conditions	Lateral boundary conditions	Land surface model
Thompson	Goddard	RRTM	0000 UTC ARPS _a	0000 UTC NAM _f	Noah

period from late April through mid-June. For this study, only the 24-h lead time forecasts are considered. ICs and LBCs (3-h updates) were from the 12-km grid spacing NAM model analyses and forecasts, respectively. Reflectivity data from up to 140 Weather Surveillance Radar-1988 Dopplers (WSR-88Ds) and other traditional data, such as surface observations, rawinsondes, and wind profilers, were assimilated into ICs of the simulations using the Advanced Regional Prediction System (ARPS) three-dimensional variational data assimilation (3DVAR; Xue et al. 2003; Gao et al. 2004) and cloud analysis (Xue et al. 2003; Hu et al. 2006) system. Another member that did not use the 3DVAR system is also examined in some of the case study analyses. IC perturbations were derived from evolved (through 3 h) perturbations of 2100 UTC initialized members of NCEP's Short-Range Ensemble Forecasting (SREF) system (Du et al. 2006) and added to the control member ICs. For each perturbed member, the SREF member used for the IC perturbations was also used for the LBCs.

For identifying observed dryline locations, the 20-km grid spacing Rapid Update Cycle (RUC) model analyses from NCEP (Benjamin et al. 2004a,b) were used following Coffey et al. (2013). These analyses are generated using hourly intermittent 3DVAR cycles in which recent observations from various sources (e.g., wind profilers, radar, aircraft, METARs, satellites, etc.) are assimilated using the previous 1-h RUC model forecasts as the background. On 1 May 2012 the Rapid Refresh replaced the RUC as the NOAA hourly updated assimilation/modeling system at NCEP (Brown et al. 2012). Given the frequent data assimilation cycles and relatively dense network of surface observations over the southern plains, where drylines are most common, it is expected that the RUC analyses accurately and reliably depict the observed dryline positions. The accuracy of the dryline positions depicted by RUC analyses was confirmed through some simple comparisons between dryline positions manually determined from surface data charts and the dewpoint fields in the RUC (not shown). Coniglio (2012) documented a slight moist bias near the surface in RUC analyses (~ 0.7 K) with no systematic temperature biases. However, there is no reason to believe that these small moisture biases would affect the dryline position, which is determined by dewpoint differences many times greater in magnitude than the moist biases in the RUC.

b. Dryline identification

In the 24-h PBL member forecasts and corresponding RUC analyses, dryline positions were determined using the manual identification procedure developed by Coffey et al. (2013). The main criterion for dryline classification

was an unambiguous boundary between relatively moist and dry air with along-boundary length scales $O(100)$ km. Moisture boundaries were identified using the 2-m specific humidity field and it was required that at some point along the boundary the specific humidity gradient magnitude was at least $3 \text{ g kg}^{-1} (100 \text{ km})^{-1}$. In addition, the 2-m temperature field was used to distinguish drylines from cold fronts. Moisture boundaries clearly resulting from convective outflow were not considered. Finally, a shift in the 10-m wind direction from a dry to a moist source region was required. The existence of this shift was subjectively determined. Dryline identification was performed over the domain bounded by 30° – 43° N, 106° – 90° W.

For cases in which dryline criteria were met, a Grid Analysis and Display System (GrADS; <http://www.iges.org/grads/>) script was used to manually draw a series of points along the axis of maximum specific humidity gradient magnitude. Straight-line segments connecting these points composed the dryline, and corresponding latitude–longitude coordinates were output to files for subsequent analysis. To compute average dryline longitude, the midpoint longitude of each line segment composing the dryline was computed. Then, weights were assigned to each midpoint longitude based on the ratio of the corresponding segment length to that of the entire dryline, and the average dryline longitude was computed as the weighted average of the midpoint longitudes. For reference, at the northernmost, middle, and southernmost latitudes of the analysis domain, 1° longitude corresponds to 81.3, 89.4, and 96.3 km, respectively.

To account for the differences in scales between the 4-km grid spacing forecasts and the 20-km grid spacing RUC analyses, a Gaussian-weighted filter was used to dampen wavelengths below 120 km in the specific humidity field before computation of gradient magnitudes. Coffey et al. (2013) found that application of this filter smoothed out finescale structures in the gradient fields while retaining and oftentimes emphasizing the dryline position, which was especially important for the higher-resolution WRF Model simulations. For further details on the procedure and examples of its application, see Coffey et al. (2013).

Over the period from late April through mid-June 2010–12, 40 cases in which drylines were present in all PBL members and the RUC analyses were identified. Because the SREF system was not run on weekends, these 40 cases do not represent all the dryline cases that occurred during this period. The 40 cases include 10 during 2010 (30 April; 7, 11–13, 20, 22, and 25 May; and 12 and 18 June; drylines were present at 0000 UTC on these dates), 14 during 2011 (30 April; 10–13, 18–21, 24–25, and 28–31 May; and 9 June), and 16 during 2012 (26 and 28 April; 1–2, 4–5, 19, 23–26, 28, and 30–31 May; and

0000 UTC 13 May 2010

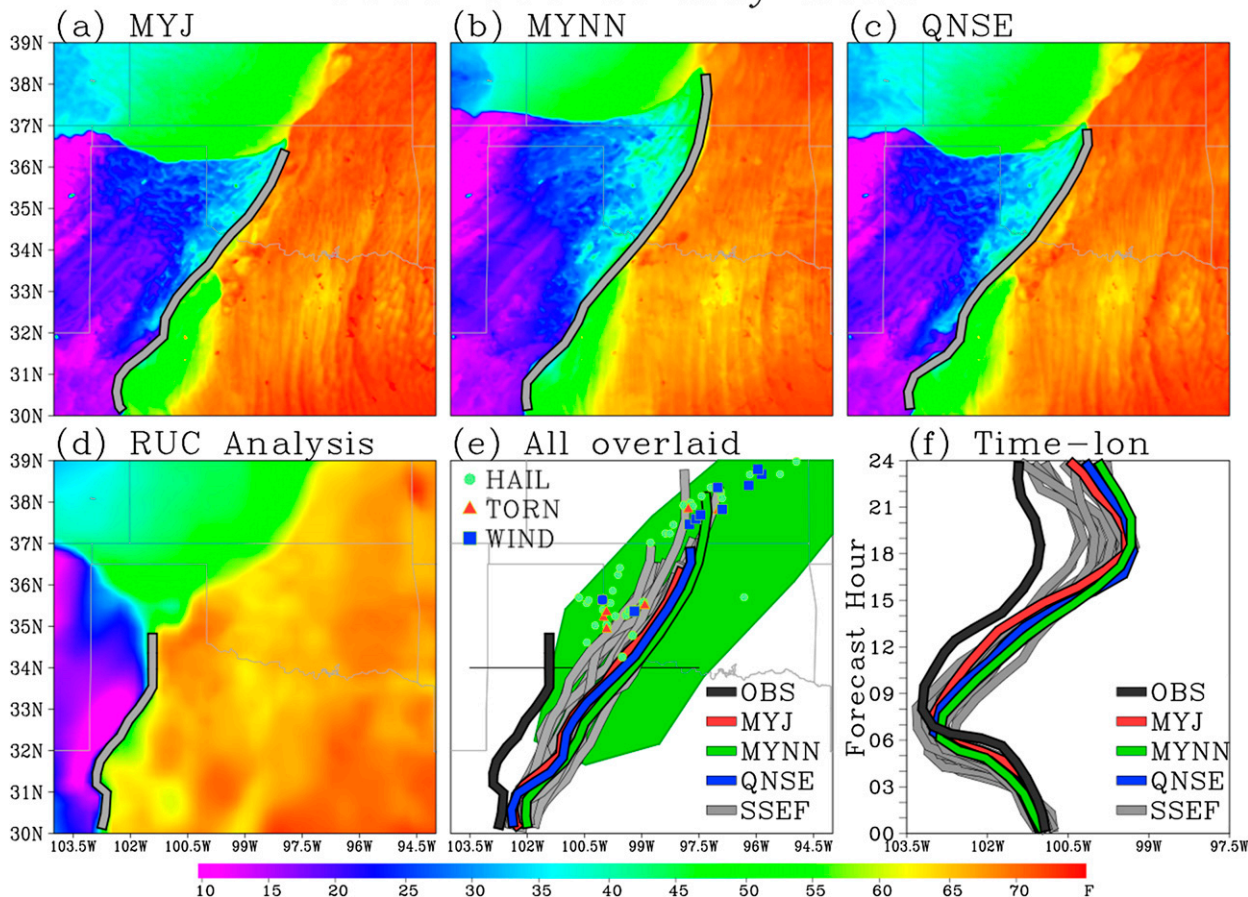


FIG. 1. Dewpoint ($^{\circ}\text{F}$; shaded) valid at 0000 UTC 13 May 2010 with manually defined dryline locations denoted by gray lines for 24-h forecasts from (a) MYJ, (b) MYNN, (c) QNSE, and (d) the RUC analysis. (e) Dryline locations for (a)–(d) are shown (colored lines) along with all other non-PBL SSEF system members (gray lines; legend at bottom right). The green-shaded region indicates a “slight” risk for severe weather as determined by SPC as part of their severe weather outlook issued at 2000 UTC 12 May 2010. Locations of severe storm reports that occurred within a 6-h window centered at 0000 UTC 13 May 2010 are marked (legend at top left). The black horizontal line at 34°N denotes the area used in (f). (f) Time–longitude plot of forecast and observed dryline locations at 34°N from 0000 UTC 12 May to 0000 UTC 13 May 2010.

10 and 11 June). Because the PBL members from all three years include the MYJ, MYNN, and QNSE schemes, there is a sample size of 40 cases for comparing these members. The PBL ACM2 and YSU schemes were only run during 2011 and 2012, so there is a sample size of 30 cases for comparing these members, and YSU-T was only run during 2011 for a sample size of 14 cases.

3. Results

a. Example cases

Figures 1–5 illustrate dewpoint fields and dryline positions for two representative cases, which were chosen because they depict drylines associated with a range of severe weather risks [e.g., slight risk on 12 May 2010 (Fig. 1), and high risk on 24 May 2011 (Fig. 4)].

Furthermore, as will be shown in subsequent analyses, there was an overall eastward bias in forecast dryline positions, and both of these cases contain this eastward bias.

1) 12 MAY 2010

A cutoff midtropospheric low embedded within a broad midtropospheric trough progressed slowly eastward during 12–13 May, roughly covering the western half of the United States. Downstream of the trough, a broad region of southwesterly 500-hPa winds >50 knots (kt; $1 \text{ kt} = 0.51 \text{ m s}^{-1}$) extended from northern Texas and western Oklahoma into Kansas, northern Missouri, eastern Nebraska, and Iowa (not shown). At the surface, a frontal boundary was stretched across northern Missouri, eastern Kansas, and northwestern Oklahoma, and into the Texas Panhandle, with a dryline extending south across western Texas (Fig. 1d). Because

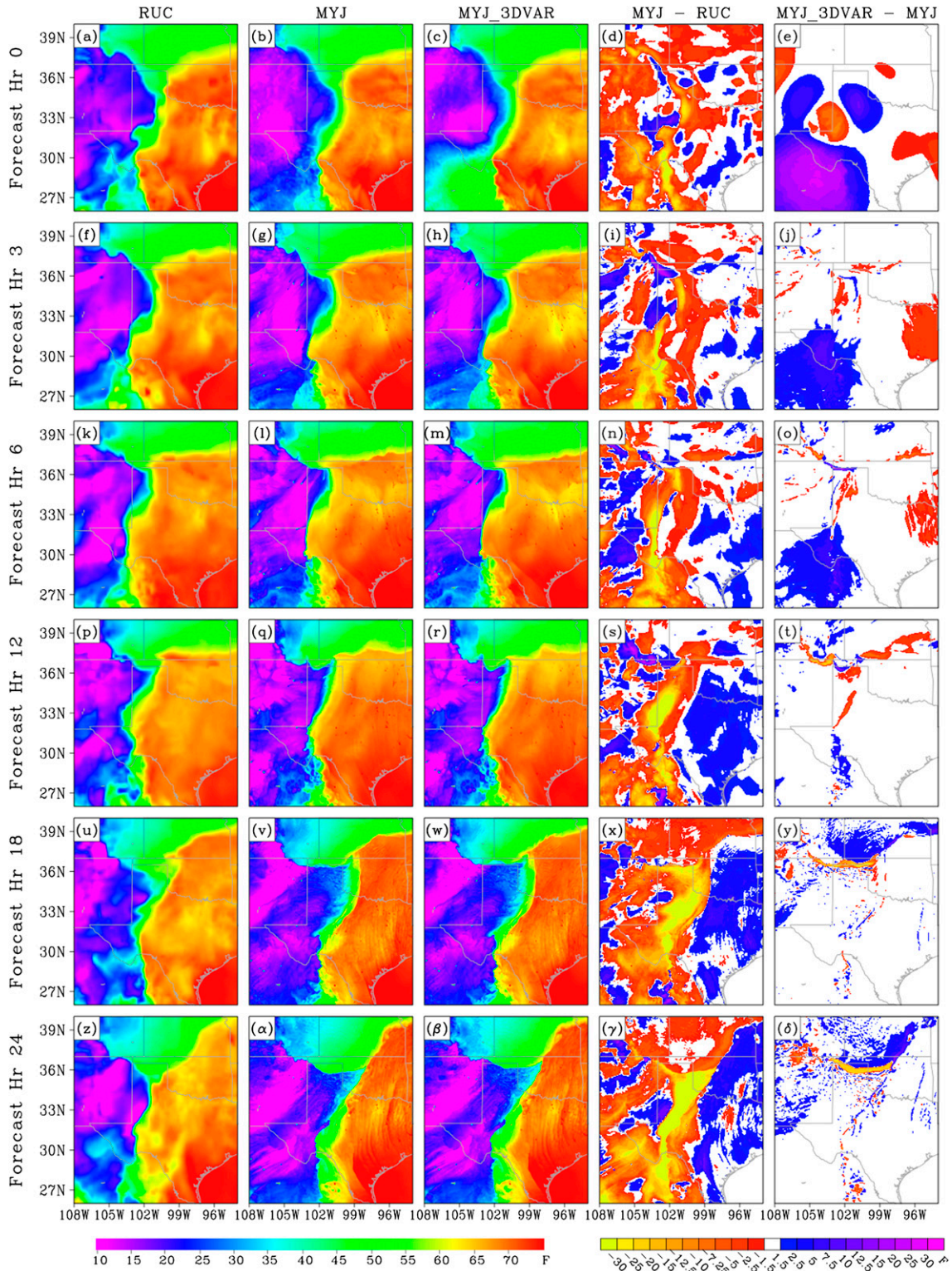


FIG. 2. Dewpoint ($^{\circ}$ F; shaded) valid at 0000 UTC 12 May 2010 (forecast hour 0) from (a) the RUC analysis, (b) MYJ without 3DVAR, and (c) MYJ with 3DVAR. (d) Dewpoint difference between MYJ without 3DVAR and the RUC analysis, and (e) dewpoint difference between MYJ with 3DVAR and MYJ without 3DVAR. (f)–(j), (k)–(o), (p)–(t), (u)–(y), (z)–(δ) As in (a)–(e), but for forecast hours 3, 6, 12, 18, and 24, respectively.

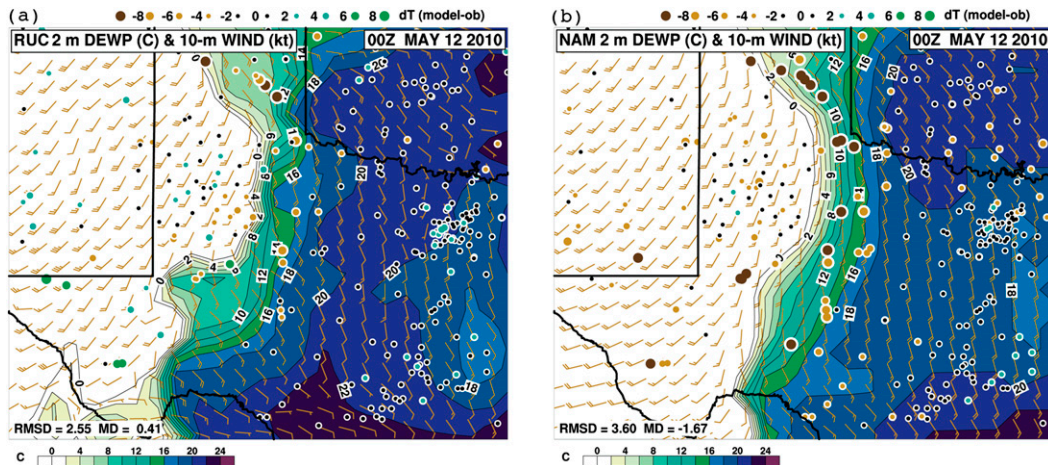


FIG. 3. Dewpoint ($^{\circ}\text{C}$; shaded) and 10-m wind barbs (kt) valid at 0000 UTC 12 May 2010 from (a) the RUC analysis and (b) NAM. The differently colored and sized dots depict locations of observations valid near the corresponding time and contained in the MADIS dataset. Larger dot sizes indicate larger differences between the MADIS observations and the nearest analysis grid point, with the brown (green) shades indicating the analysis is dry (moist) relative to the MADIS observations. A legend for the dots is provided at the top.

of sufficient deep-layer vertical shear and convective instability for severe storms east of the frontal boundary and dryline, SPC issued a slight risk for much of this region. Around 2000 UTC a broken line of storms formed in south-central Kansas along the frontal boundary, producing a couple tornadoes and numerous severe hail and wind reports (Fig. 1e). By 2200 UTC, another broken line of storms that produced severe hail and a few tornadoes had formed along the northern part of the dryline in the eastern Texas Panhandle. Finally, around 0200 UTC another round of storms formed in the Texas Panhandle near the triple point (i.e., intersection of warm and dry, warm and moist, and cool and dry air masses to the west, east, and north of the dryline, respectively) as the frontal boundary began to move south.

The dryline position in this case (along with the frontal boundary) played an important role in where storms and associated severe weather occurred, and the particularly large 24-h forecast dryline position errors (e.g., Fig. 1e) could have mislead forecasters into believing the severe weather threat was farther east than in reality. The easternmost extent of the dryline identified in the RUC analyses at 0000 UTC 13 May was about 101.5°W , while that of the forecast drylines was about 98.0°W . The average eastward errors for MYJ, QNSE, and MYNN were 1.9° , 2.1° , and 2.8° , respectively. There were also very noticeable differences in the northernmost extent of the forecast and observed drylines, which was related to the position of the southwest–northeast-oriented frontal boundary to which the dryline was attached forming the triple point. The farther east the

dryline mixed, the farther northeast along the frontal boundary the triple point became positioned. In the MYJ and QNSE simulations (Figs. 1a and 1c, respectively), the frontal boundary position was well forecast; thus, the position of the triple point was mostly only affected by the eastward dryline position error. However, in the MYNN simulations (Fig. 1b), the frontal boundary was positioned too far north, exacerbating the northward position error of the forecast triple-point position in east-central Nebraska, which was about 400 km from the observed triple point in the Texas Panhandle. The 24-h forecast dryline positions for non-PBL SSEF system members (gray lines in Fig. 1e) also incorrectly simulated the westward extent of the observed dryline position.

For further insight into the dryline position errors and their evolution in the 24-h forecast, a time–longitude plot of observed and forecast dryline positions at 34°N is shown in Fig. 1f. As in the spatial plots, the drylines in time–longitude space were manually identified using the axis of the maximum specific humidity gradient magnitude. During the first 9 h of the forecast (lower part of Fig. 1f), the dryline in the RUC analyses retreated westward. Then, after 0900 UTC, the RUC dryline moved eastward until 1800 UTC, after which it retreated slightly westward again. This east–west diurnal variability is typical of drylines and the forecast dryline east–west diurnal variation follows a similar pattern. However, there is a surprisingly large difference in the dryline longitude at the forecast initialization time with the RUC dryline about 0.75° to the west of the SSEF member drylines. This difference can be seen in the

0000 UTC 25 May 2011

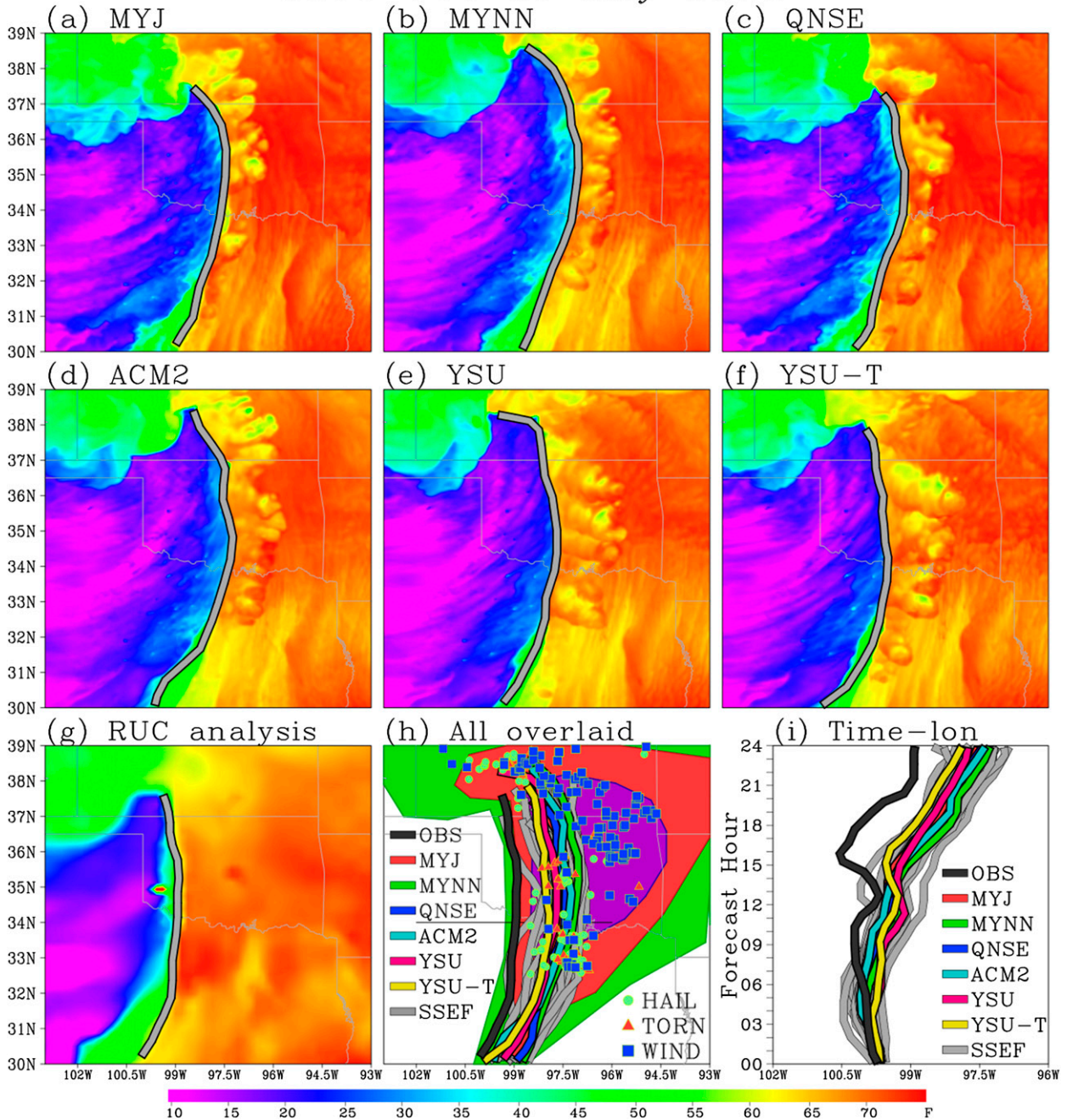


FIG. 4. Dewpoint ($^{\circ}\text{F}$; shaded) valid at 0000 UTC 25 May 2011 with manually defined dryline locations denoted by gray lines for 24-h forecasts from (a) MYJ, (b) MYNN, (c) QNSE, (d) ACM2, (e) YSU, (f) YSU-T, and (g) the RUC analysis. (h) Dryline locations for (a)–(g) are shown (colored lines) along with all other non-PBL SSEF system members (gray lines; legend at left). The green-, red-, and purple-shaded regions indicate “slight,” “moderate,” and “high” risks for severe weather as determined by SPC as part of their severe weather outlook issued at 2000 UTC 24 May 2011. Locations of severe storm reports that occurred within a 6-h window centered at 0000 UTC 25 May are marked (legend at bottom right). The black horizontal line at 34°N denotes the area used in the time–longitude section in (i). (i) Time–longitude plot of forecast and observed dryline locations at 34°N from 0000 UTC 24 May to 0000 UTC 25 May 2011.

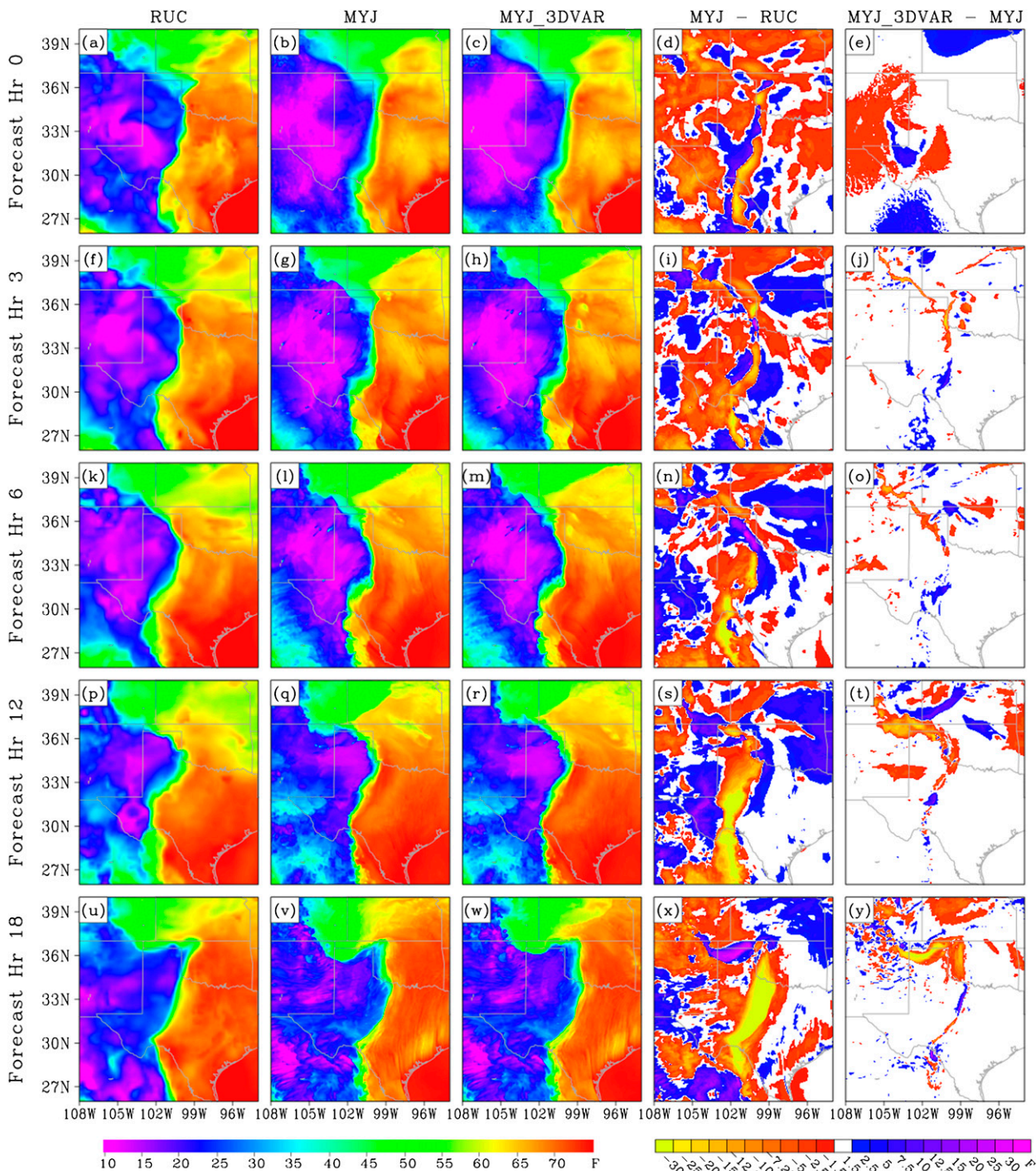


FIG. 5. Dewpoint ($^{\circ}\text{F}$; shaded) valid at 0000 UTC 24 May 2011 (forecast hour 0) from (a) the RUC analysis, (b) MYJ without 3DVAR, and (c) MYJ with 3DVAR. (d) Dewpoint difference between MYJ without 3DVAR and the RUC analysis, and (e) dewpoint difference between MYJ with 3DVAR and MYJ without 3DVAR. (f)–(j), (k)–(o), (p)–(t), (u)–(y) As in (a)–(e), but for forecast hours 3, 6, 12, and 18, respectively.

lower part of Fig. 1f, as well as by comparing the 2-m dewpoint from the RUC analysis valid 0000 UTC 12 May (Fig. 2a) to that of MYJ without (Fig. 2b) and with (Fig. 2c) 3DVAR and cloud analysis (MYJ without data

assimilation is just the downscaled NAM analysis). It appears that this initial offset, combined with the forecast drylines not retreating far enough west during 0–9-h forecast period and then mixing too far east during the

9–18-h forecast period, led to the very large errors in the 24-h forecast.

Furthermore, the MYJ forecasts were generally much drier than corresponding RUC analyses in much of northern Mexico, far southwestern Texas, and eastern New Mexico, which can be seen from 2-m dewpoint difference plots between MYJ and RUC (Figs. 2d,i,n,s,x,y). In these plots, MYJ without 3DVAR is used because it was found that the impact of 3DVAR on the 2-m dewpoint field greatly diminishes just 12 h into the forecast, which can be seen in the 2-m dewpoint difference plots between MYJ with and without the 3DVAR and cloud analysis (Figs. 2e,j,o,t,y,δ). Notice that 3DVAR adds a large area of increased moisture from northern Mexico to southwestern Texas (Fig. 2e), but this increased moisture quickly dissipates. The increased moisture there suggests that there were observations supporting its presence, but that the overriding influence of the NAM ICs and LBCs eliminated its influence later in the forecast. Thus, we suspect that a dry bias in the NAM also contributed to the large forecast dryline errors. Further supporting the dry NAM bias, Fig. 3b shows the 2-m dewpoint from the 0000 UTC 12 May NAM analysis, with dots overlaid at the locations of surface observations. The size and color of the dots indicates the difference between the observations and the nearest grid point of the NAM analysis. Along and west of the moisture gradient there is a particularly noticeable dry bias in the NAM analysis, with a mean dewpoint difference between the observations and the NAM analysis of -1.67°C . The RUC analysis 2-m dewpoint (Fig. 3a) is a better match with the observations, but with a slight moist bias (mean dewpoint difference between the observations and the RUC analysis is 0.41°C).

2) 24 MAY 2011

A high-amplitude midtropospheric short-wave trough moved rapidly eastward into the southern high plains during the afternoon of 24 May with an associated dryline that had progressed to western Oklahoma by 2100 UTC. The air mass to the east of the dryline was extremely unstable and collocated with strong upper-level flow that veered with height, creating favorable conditions for severe weather, including strong long-track tornadoes and large hail. Accordingly, SPC issued a “high” risk for severe weather in their day 1 outlooks (Fig. 4h). Around 1900 UTC, the first dryline-initiated storms formed in southwestern Oklahoma and quickly moved northeast. By 2100 UTC, storm coverage along the dryline had increased dramatically with a broken line of supercells stretching along and just east of the dryline from south-central Kansas, through western

Oklahoma, and into northern Texas (not shown). Some of the supercells produced violent, long-track tornadoes.

Again, the dryline position played an important role in where storms and the associated severe weather occurred, and, similar to 12 May 2010, there were particularly large 24-h forecast dryline position errors (e.g., Fig. 4h). The easternmost extent of the dryline identified in the RUC analyses at 0000 UTC 25 May was about 99.0°W , while SSEF member drylines extended east as far as 96.75°W . From smallest to largest, the average eastward errors for YSU-T, YSU, ACM2, MYJ, QNSE, and MYNN were 0.8° , 1.0° , 1.2° , 1.2° , 1.3° , and 1.6° , respectively. Similar to 12 May 2010, in addition to having the largest eastward dryline position errors, MYNN also placed the triple point much farther north into central Kansas relative to observations and the other PBL members.

The time–longitude plot of observed and forecast dryline positions at 34°N (Fig. 4i) shows that, unlike on 12 May 2010, the dryline longitude at the initialization time in the RUC and NAM analyses lines up quite well. During the first 15 h of the forecast, the dryline in the RUC analyses slowly moved westward, with a brief excursion to the east and retreat back to the west between 1200 and 1500 UTC. Then, between 1500 and 2100 UTC, the RUC dryline mixed eastward and remained virtually stationary from 2100 to 0000 UTC. The dryline longitudes in the PBL members line up well with the RUC analyses up until about 6 h into the forecast. Then, instead of continuing to slowly move westward, the PBL member drylines begin to move eastward and by 1500 UTC there are already significant eastward position errors relative to the RUC analyses. After 1500 UTC, the RUC analyses and PBL member drylines mix eastward at about the same speed, but instead of stopping at 2100 UTC, as in the RUC analyses, the forecast drylines in all the PBL members continue to mix east until 0000 UTC.

Comparing the 2-m dewpoint from the RUC analysis valid at 0000 UTC 24 May (Fig. 5a) to that of MYJ without (Fig. 5b) and with (Fig. 5c) the 3DVAR and cloud analysis system, there is a general dry bias in MYJ relative to the RUC over far southwestern Texas and the Texas Panhandle, as well as New Mexico (see Fig. 5d). Also, the southern portion of the dryline in the RUC analysis has a tighter moisture gradient and extends farther west relative to the MYJ analyses, which is reflected in the difference plots by the adjacent axes of positive and negative moisture differences in west-central Texas (Fig. 5d). These negative moisture differences can be tracked through time (Figs. 5d,i,n,s,x); thus, similar to the 12 May 2010 case, we suspect that the dry bias in the NAM analysis contributed to the dryline errors.

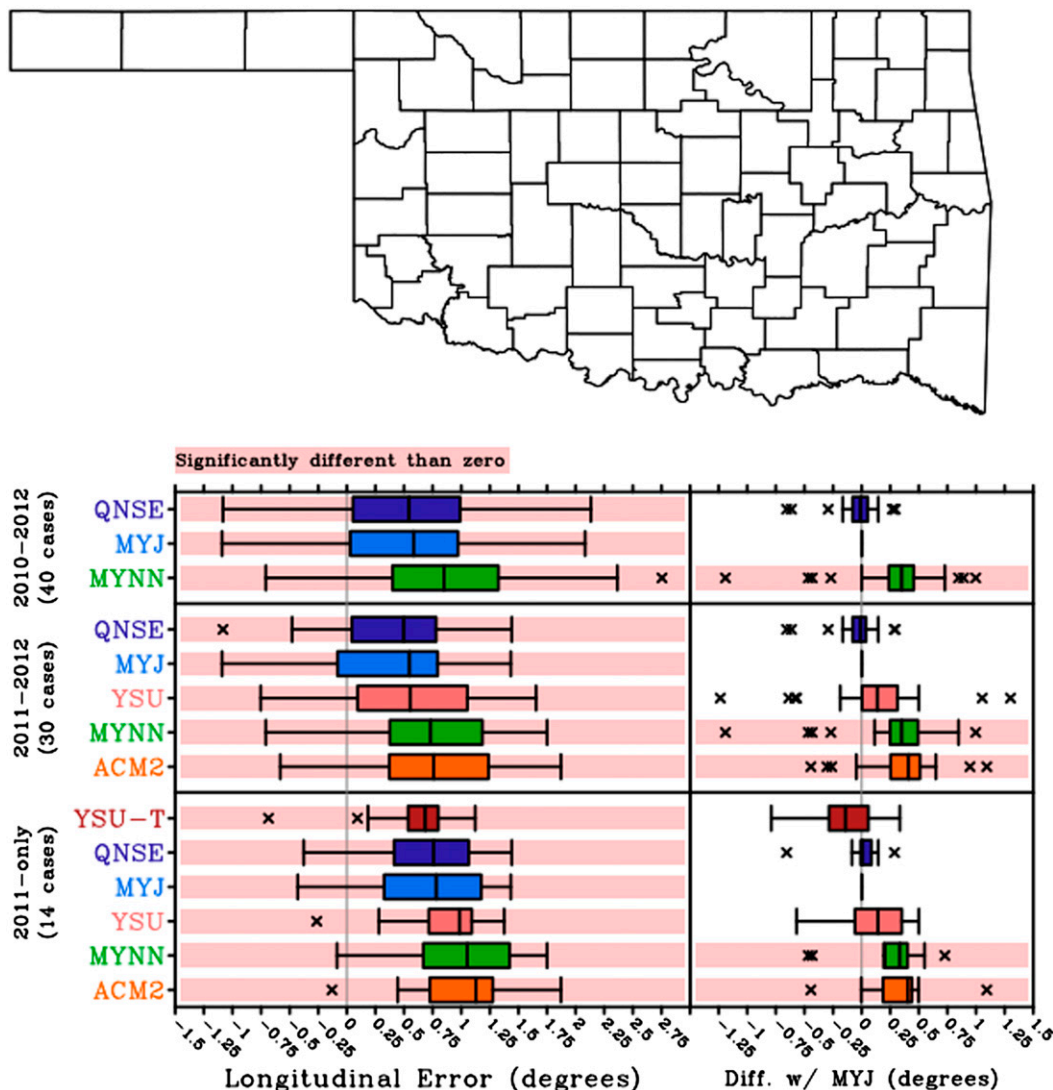


FIG. 6. (top) A map of Oklahoma is shown for reference; its horizontal scale matches that of the x axis for the box plots. (bottom) Box plots for the distribution of average longitudinal dryline position errors for the sets of cases covering 2010–12, 2011–12, and 2011 only are given on the left. Box plots for the differences in dryline position with respect to MYJ are given on the right. The IQR within each box plot is colored according to the particular boundary layer scheme (indicated along the y axis). The underlain pink shading indicates that differences with respect to the observations (on the left) or MYJ (on the right) were statistically significant at $\alpha = 0.05$. The median is indicated by the straight black line through each box, where the box encompasses the IQR, outliers defined by values outside of 1.5(IQR) are marked by crosses, and horizontal lines (whiskers) denote the smallest and largest values that are not outliers.

b. Aggregate dryline statistics

For a robust statistical analysis of average dryline position errors, Fig. 6 (bottom) shows box plots constructed using the distributions of average longitudinal dryline errors in the PBL members. For the three PBL members that could be compared from the 2010–12 sample of 40 cases [first three box plots in Fig. 6 (bottom)], there was a clear eastward bias in 24-h forecast

dryline position with the mean eastward error of all three being significantly different from zero [indicated by pink shading in Fig. 6 (bottom)]. In fact, the entire interquartile range (IQR) in all three box plots is greater than zero. The QNSE and MYJ members had similar distributions with median eastward errors just above 0.5° , while MYNN had a median eastward error of about 0.90° . From the box plots on the right side of Fig. 6 (bottom), the differences relative to MYJ for QNSE were

distributed around zero, while for MYNN the median difference was about 0.30° , and there was only one case in which MYNN had a dryline west of that from MYJ.

For the five PBL members for the April–June 2011–12 sample of 30 cases, again, there was a clear eastward bias in forecast dryline position, with median eastward errors ranging from about 0.40° in QNSE and MYJ to about 0.60° – 0.75° in YSU, MYNN, and ACM2. The MYNN and ACM2 drylines tended to be farthest east relative to MYJ, while the YSU drylines were to the east, but not as far as MYNN and ACM2. Relative to MYJ, the mean differences in average dryline longitude for MYNN, ACM2, and YSU were all significantly different than zero.

Finally, for the six PBL members for the 2011 sample of 14 cases, the eastward bias was present and was the largest among the three sets of cases examined. However, the relative differences among the PBL members are similar to the other sets of cases. The dryline errors for the YSU-T member, which was only run during 2011, were particularly notable because they tended to be west relative to the MYJ member, which was the only scheme for which this was the case in the entire dataset. The average dryline differences between the YSU and YSU-T member were statistically significant; however, the YSU-T average dryline differences relative to MYJ were not statistically significant.

c. Impact of IC errors on forecast dryline errors

For 12 May 2010 and 24 May 2011, the eastward dryline errors seemed closely related to a dry bias in the NAM ICs. To further investigate whether IC errors played a role in dryline errors for the other cases, average 2-m dewpoint biases were computed over the region from 29° to 39°N and 105° to 99°W . This area was chosen because it appeared to be where dry biases were largest in the case studies. The 2-m dewpoint errors were computed using surface observations from the Meteorological Assimilation Data Ingest System (MADIS; Miller et al. 2005, 2007). For each surface observation within the bounded region, the difference between the 2-m dewpoint of the MADIS observation and that of the nearest grid point of the NAM ICs was computed. Then, the bounded region was divided into 1.0° latitude \times 1.0° longitude squares, and average differences were computed over each square so that areas with more dense observations would not be given disproportionate weight. Finally, an average 2-m dewpoint error was computed by averaging over all the $1.0^\circ \times 1.0^\circ$ squares.

To test the impact of the NAM 2-m dewpoint errors on the forecast dryline positions, scatterplots were created in Fig. 7 by plotting the average error over the bounded region against the average longitudinal dryline position error for each case. The scatterplots were only

created for the members that were available from all 40 cases. The correlation coefficients R were computed using the `cor.test()` function from the R statistical software package (R Development Core Team 2013). The correlation coefficients were -0.44 , -0.46 , and -0.48 , for the MYJ, QNSE, and MYNN members, respectively, all of which were highly significant with p values ≤ 0.005 . Best fit lines computed using linear regression are also shown in Fig. 7. Thus, there is strong evidence that systematic errors in the 2-m dewpoint analysis of the NAM explain much of the forecast dryline position errors. Physically, this makes sense, as a drier initial state should result in greater sensible heat flux and stronger vertical mixing, which would tend to push the dryline farther east. It is also possible that the dryline itself is too far east in the NAM analyses, which should also contribute to eastward position errors later in the forecast.

The MYJ and QNSE schemes contained a very similar relationship between the NAM IC 2-m dewpoint bias and forecast dryline error (Fig. 7d), which is not surprising since in the previous sections it was found that these two schemes behave very similarly. For MYNN, the slope of the best fit line was almost identical to that of MYJ and QNSE, but shifted to greater dryline errors by about 0.30° , consistent with the results in Fig. 6. Of particular interest in Fig. 7d is the longitudinal dryline error for a dewpoint bias of zero (i.e., the y intercept). For MYJ and QNSE, the y intercept is about 0.30° , while for MYNN it is about 0.60° . This means that, even when the NAM IC 2-m dewpoint is unbiased, there is still a systematic eastward bias in the forecast dryline positions, which is most pronounced in MYNN. The dryline error present when the 2-m dewpoint bias is near zero can be attributed to the PBL schemes or other aspects of the WRF Model formulation.

d. Dryline position errors by year

In Fig. 8, the average 2-m dewpoint errors for each year are shown over the bounded region described in the previous section, along with corresponding box plots of dryline errors for MYJ, QNSE, and MYNN. The average 2-m dewpoint errors for 2010 and 2011 were -2.05° and -1.27°C , respectively, and both years had clear eastward biases in 24-h forecast dryline position. However, in 2012, the 2-m dewpoint biases were near zero, with corresponding eastward dryline position errors in all three PBL members that were noticeably smaller than in 2010 and 2011. In MYJ and QNSE, the median dryline errors were near zero during 2012, while in MYNN they were about 0.60° .

It is likely that the reduction in the 2-m dewpoint bias of the NAM ICs was related to a major upgrade of the NAM model and data assimilation system that occurred

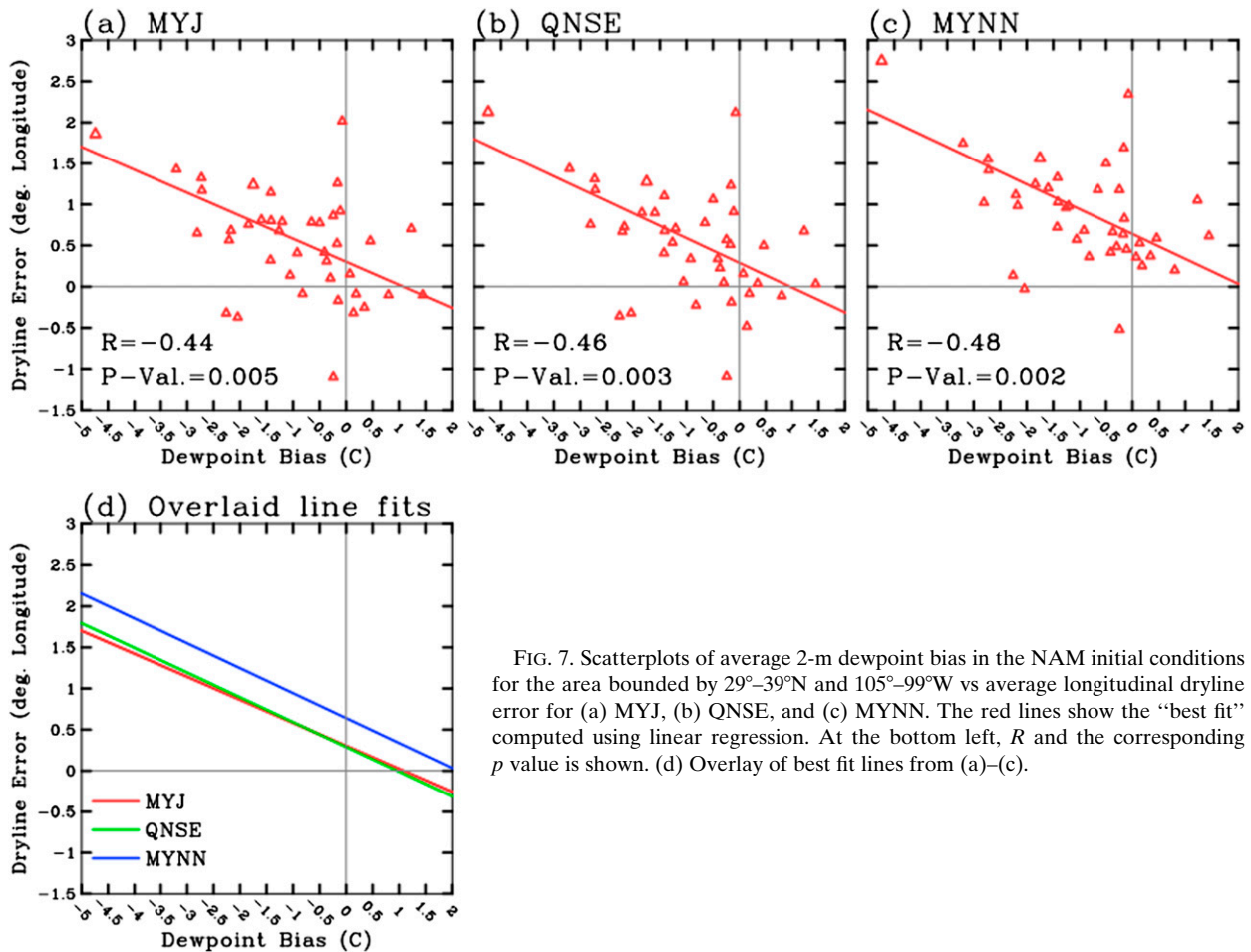


FIG. 7. Scatterplots of average 2-m dewpoint bias in the NAM initial conditions for the area bounded by 29°–39°N and 105°–99°W vs average longitudinal dryline error for (a) MYJ, (b) QNSE, and (c) MYNN. The red lines show the “best fit” computed using linear regression. At the bottom left, R and the corresponding p value is shown. (d) Overlay of best fit lines from (a)–(c).

during October 2011. For this upgrade, a new modeling framework known as the NOAA Environmental Modeling System (NEMS) was implemented and modifications were made to the NAM Data Assimilation System (NDAS) that uses the Gridpoint Statistical Interpolation analysis system (GSI). The NDAS changes included assimilation of new observations from numerous different platforms, as well as updating the 2-m temperature and dewpoint fields (before the update, the 2-m temperature–moisture fields were simply the first guess from the previous model cycle). A summary of these changes can be found online (http://www.nws.noaa.gov/os/notification/tin11-16nam_changes_aad.htm).

e. Vertical structure of drylines and the near-dryline environment

To further investigate how the various PBL schemes depict the PBL and how these depictions may be related to the dryline position errors, dryline-relative composite vertical cross sections of the near-dryline environment were constructed for each PBL member. At 0.15° latitude increments along the dryline, vertical cross sections

of selected fields are extracted up to model level 35 (~200 hPa) from 2.0° west of the dryline to 4.0° east of the dryline. Then, a composite cross section for each case is taken by averaging over all these individual cross sections, and a single composite cross section for each PBL member is taken by averaging the composites over all the cases. Composite vertical cross sections of specific humidity, temperature, pressure, vertical velocity, and wind magnitude were examined. Figure 9 illustrates how this procedure was implemented for MYJ and MYNN forecasts initialized on 10 May 2010. The composite cross sections smooth out some of the tight vertical gradients in specific humidity that can be seen in the individual cross sections, but the main characteristics of the PBL are retained. For example, comparing Fig. 9e (MYJ) with Fig. 9j (MYNN), it is easily seen that MYJ has a PBL that is shallower and moister than MYNN.

Vertical cross-sectional composites from each PBL member available during the 2011–12 period (30 cases) are shown in Fig. 10. This specific period was chosen for examination because there is a large sample for which five out of the six PBL members were available. For

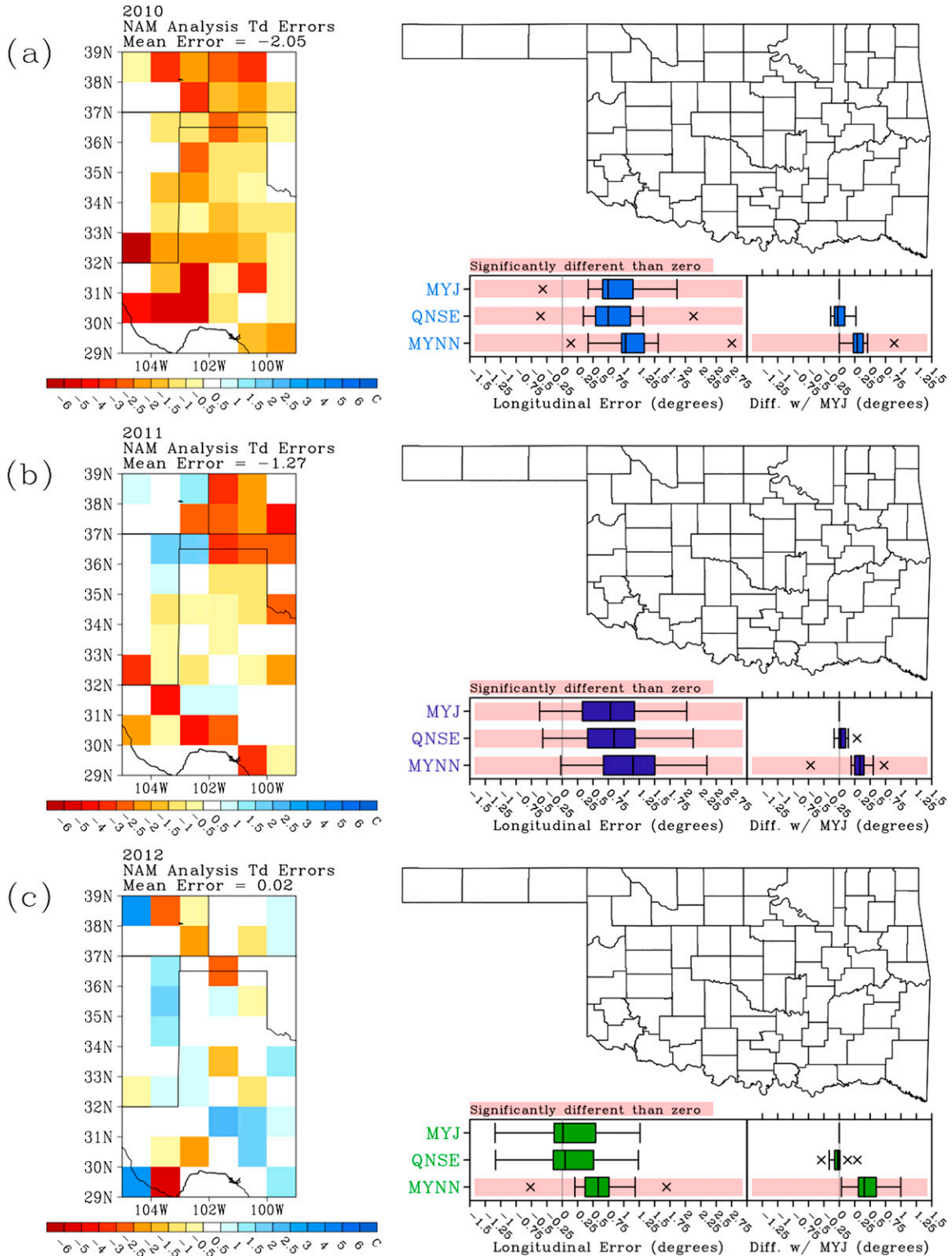
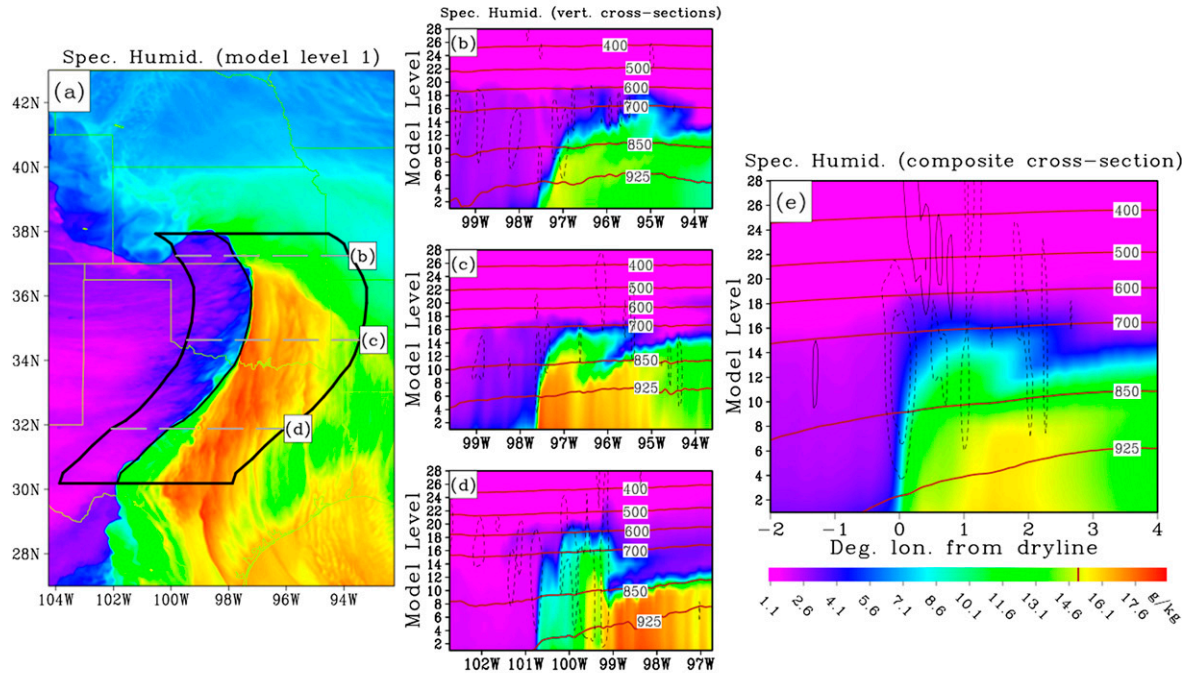


FIG. 8. (a) Mean 2-m dewpoint errors in the NAM ICs for the 2010 dryline cases (on the left) and box plots for the distribution of average longitudinal dryline position errors for the 2010 cases (on the right). The box plots are constructed similarly to those in Fig. 6. (b),(c) As in (a), but for 2011 and 2012, respectively.

MYJ COMPOSITE EXAMPLE – 0000 UTC 11 May 2010



MYNN COMPOSITE EXAMPLE – 0000 UTC 11 May 2010

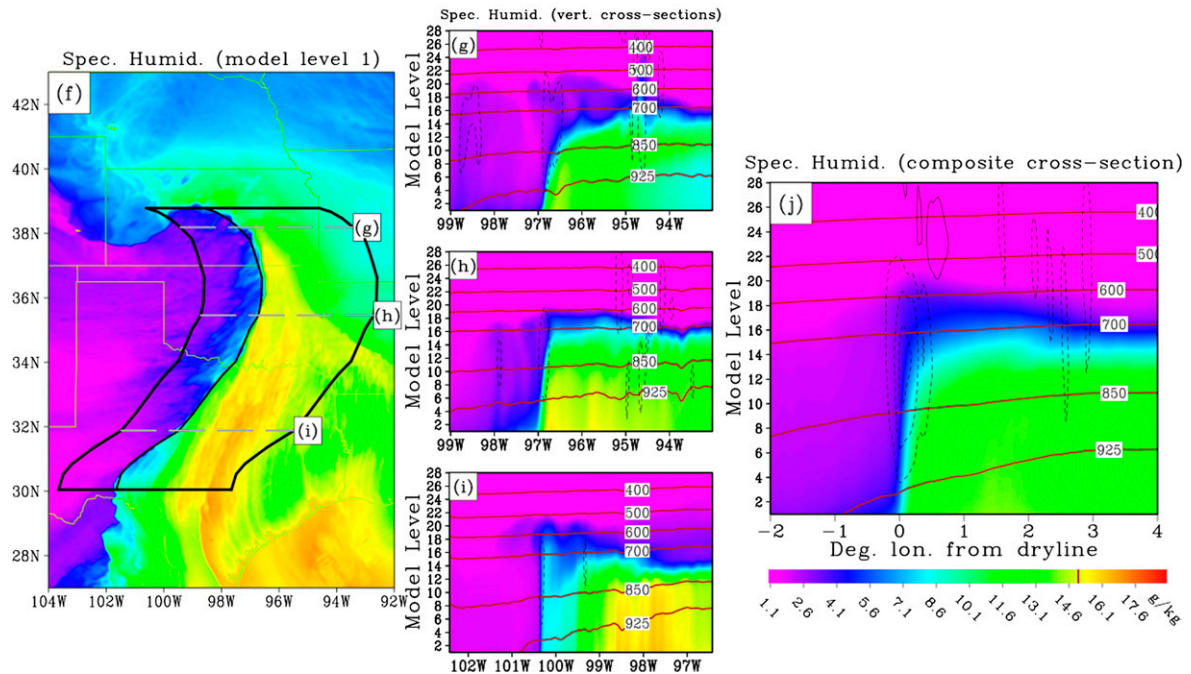


FIG. 9. (a) Specific humidity (g kg^{-1} ; shaded) at the lowest model level in the 24-h forecast from the MYJ member valid at 0000 UTC 11 May 2010. The thick black line encloses the area over which a composite dryline cross section was constructed. The thin black line inside of this area marks the dryline. (b),(c),(d) Individual vertical cross sections of specific humidity (shaded) and pressure (red contours) for locations indicated by horizontal gray dashed lines and labeled b, c, and d in (a), respectively. (e) Composite vertical cross section of specific humidity and pressure constructed by taking the average of cross sections anchored every 0.15° in latitude along the dryline. (f)–(j) As in (a)–(e), but for the MYNN member.

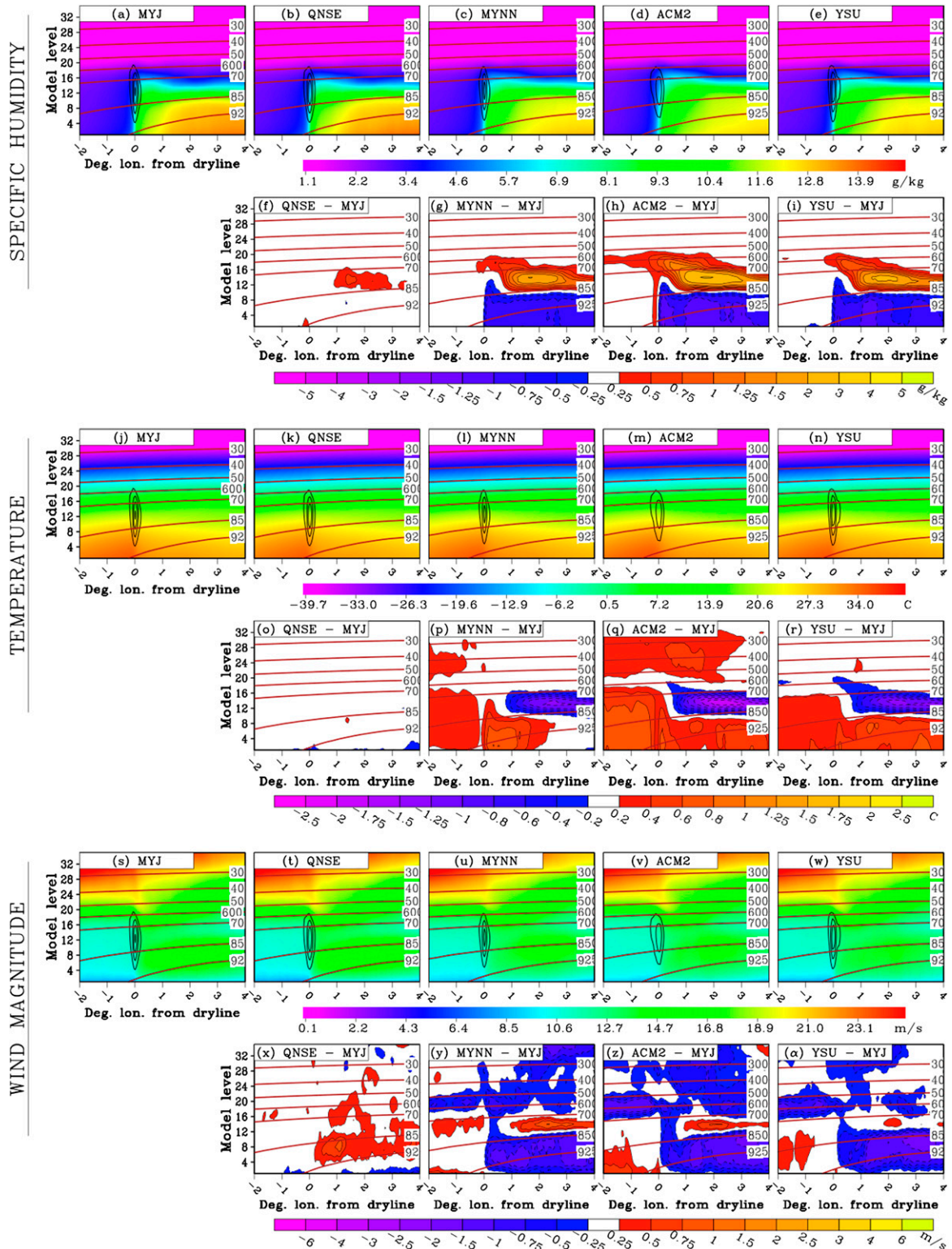


FIG. 10. Composite vertical cross sections of specific humidity (g kg^{-1} ; shaded), pressure (hPa; red contours), and upward vertical velocity (Pa s^{-1} ; black contours at 1 Pa s^{-1} interval from -1 to -6 Pa s^{-1}) over all 2011–12 cases for (a) MYJ, (b) QNSE, (c) MYNN, (d) ACM2, and (e) YSU. Pressure (hPa; red contours) and specific humidity difference relative to MYJ (g kg^{-1} ; shaded) are given for (f) QNSE, (g) MYNN, (h) ACM2, and (i) YSU. (j)–(r), (s)–(α) As in (a)–(i), but for temperature and wind magnitude, respectively.

specific humidity (Figs. 10a–e), the vertical extent of the dryline, as well as the interface between the PBL and elevated mixed layer, stand out very clearly. To more clearly illuminate differences among the members, Figs. 10f–i show differences in specific humidity relative to MYJ. Differences are shown relative to MYJ because it is arguably the most popular PBL scheme and it has been used in the control member of the SSEF system since 2007. From the difference plots, it is clear that the vertical distribution of moisture west of the dryline is very similar in each of the five PBL members. However, east of the dryline in the moist sector there are much more noticeable differences in the vertical moisture distribution. QNSE has the smallest moisture differences relative to MYJ, which is not surprising because the two schemes are formulated similarly.

Specific humidity differences relative to MYJ in MYNN, ACM2, and YSU are much larger than those of QNSE and all exhibit a very similar pattern. In the layer closest to the ground, these members are drier than MYJ, while between about 850 and 700 hPa they are moister. This pattern is consistent with a deeper and overall drier PBL than MYJ and closely matches the results presented in Fig. 10 of Coniglio et al. (2013). The differences are also dependent on the distance from the dryline (i.e., x axis in Fig. 10); in particular, the largest positive moisture differences centered between 850 and 700 hPa occur between 1.0° and 3.0° east of the dryline. This result is consistent with the strength of the capping inversion increasing with eastward distance from the dryline, which usually occurs because the areas well to the east of the dryline are not impacted by the dryline-induced vertical circulation. Also, oftentimes when the dryline is linked to a synoptic-scale weather system, areas farther east of the dryline are less influenced by large-scale dynamical processes (e.g., differential vorticity advection) that can contribute to eroding capping inversions. When a stronger capping inversion exists, differences in the PBL depth can result in very large moisture differences where levels in one member are within the dry and stable cap and the same levels in another member are within the well-mixed PBL.

In the temperature composites (Figs. 10j–n), the dryline is not reflected as obviously as in the specific humidity composites; however, there is a clear temperature change from warmer to cooler across the dryline boundary, which is a well-known characteristic of drylines caused by differences in sensible heat flux. In the difference plots (Figs. 10o–r), QNSE has almost undetectable differences in temperature relative to MYJ. However, much more noticeable differences exist in the other three PBL members and, similar to the specific humidity composites, the patterns in these members

have some similarities. In the MYNN, ACM2, and YSU the largest negative temperature differences relative to MYJ occur in the 850–700-hPa layer about 2.0°–3.5° east of the dryline. These negative differences reflect levels where there was a capping inversion present in MYJ, while the capping inversions in MYNN, ACM2, and YSU were weaker or completely eroded. Positive temperature differences generally existed in the layer adjacent to the ground. In MYNN, the positive differences were largest from 0° to 1° east of the dryline, in ACM2 the positive differences were largest within a deep layer from 0° to 2° west of the dryline, and in YSU the positive differences were relatively homogeneous, but tended to be slightly larger east of the dryline. The results here are consistent with an overall deeper and warmer PBL in the MYNN, ACM2, and YSU members relative to MYJ and, once again, are similar to the findings of Coniglio et al. (2013).

The differences in the dryline-relative vertical cross sections of temperature and specific humidity are consistent with the differences in average forecast dryline positions errors for the different PBL members. The tendency for some of the schemes to produce warmer, drier, and deeper PBLs implies stronger vertical mixing, which in turn should result in a farther eastward dryline position because vertical mixing is usually the dominant process governing dryline movement. For example, MYJ and QNSE depict shallower, moister, and cooler PBLs relative to the other members corresponding to more westward dryline positions, while ACM2, MYNN, and YSU depict deeper, drier, and warmer PBLs corresponding to more eastward dryline positions. However, the relationship between PBL depth–moisture–temperature and dryline position is not perfect. For example, YSU tends to depict a deeper, drier, and warmer PBL than MYNN, but the average YSU dryline position errors are not as far east as MYNN.

In the wind magnitude composites (Figs. 10s–w), wind speeds are greater in the PBL east of the dryline line than they are to the west in all five PBL members. Also, there is an extension of faster wind speeds from the upper-level jet just above and to the east of the upward branch of the dryline-induced vertical circulation. This downward extension of faster wind speeds coincides with an area of downward motion (not shown) related to the dryline-induced vertical circulation; thus, it is likely caused by downward momentum transport (the vertical circulations are examined in a subsequent section). In the difference plots (Figs. 10x–z), the main difference relative to MYJ in the QNSE member is slightly faster wind speeds between 925 and 850 hPa to the east of the dryline. In YSU, ACM2, and MYNN, wind speeds are slightly slower than MYJ in the lowest levels up to about 850 hPa east of the dryline. Additionally, these three members have areas

above the PBL where wind speeds are slower than MYJ, and a small layer between 850 and 700 hPa roughly collocated with the top of the PBL where wind speeds are faster than MYJ. The weaker PBL winds in MYNN, ACM2, and YSU are likely the result of more vertical mixing/turbulence in these schemes relative to MYJ.

To evaluate the impact of modifications designed to decrease vertical mixing made to YSU in the YSU-T member, Fig. 11 shows dryline-relative composite vertical cross sections for the MYJ, YSU, and YSU-T PBL members for 2011 (14 cases), which was the only period over which YSU-T was run. Recall that the eastward dryline position errors for YSU-T were noticeably less than YSU, and during 2011 YSU-T was the only PBL member with eastward dryline position errors smaller than MYJ (Fig. 6). Thus, one might expect that weaker vertical mixing in the YSU-T member results in a shallower, cooler, and moister PBL than YSU and MYJ. Interestingly, this is not the case; the difference plot shown in Fig. 11f indicates that specific humidity differences between YSU and YSU-T are very small and Figs. 11d and 11e show that both YSU and YSU-T have similarly deeper and drier PBLs relative to MYJ. Similarly, in the temperature composites, Fig. 11i indicates that YSU and YSU-T had only very small differences east of the dryline, and to the west of the dryline, YSU-T was slightly cooler than YSU. Finally, in the wind magnitude composites (Figs. 11m–r), YSU-T had slightly weaker winds in the PBL 1.0° – 2.0° immediately east of the dryline. Given the small differences between YSU and YSU-T, it is difficult to explain why the differences in forecast dryline positions were so dramatic. The cooler temperature profiles west of the dryline along with weaker winds east of the dryline in YSU-T are consistent with less vertical mixing in YSU-T; however, these were only very subtle differences. Further investigation beyond the scope of this study is needed to better explain the differences in forecast dryline position in YSU and YSU-T.

f. Composite sounding analysis

To complement the dryline-relative composite cross sections, 24-h composite forecast soundings are presented in Fig. 12. The composite soundings were constructed by finding an “anchor point” following the dryline 1.0° south from its northernmost latitude. Then, average dewpoint, temperature, and winds were taken from 1.0° west and 0.5° , 1.0° , 1.5° , 2.0° , and 2.5° east of this anchor point to construct the composite soundings for each member at each of these distances. Additionally, surface-based convective available potential energy (CAPE), convective inhibition (CIN), and storm-relative helicity in the lowest 100- and 300-hPa layer (SRH1 and SRH3, respectively) were computed from the composite profiles.

Rather than average over the north–south direction, as was done to create the composite cross sections, the composite soundings are constructed relative to only one point on the northern section of the dryline in order to sample the area of the moist sector most likely to be within an environment favorable for severe weather. Environments immediately to the east of northern portions of the dryline tend to be associated with greater deep-layer wind shear and smaller convective inhibition relative to southern portions of the dryline because of their closer proximity to synoptic-scale weather systems and their associated dynamics. The composite soundings are presented to provide perspective on how sensitive products relevant to severe weather forecasting are to the PBL schemes and how this sensitivity changes depending on distance from the dryline.

In the postdryline environment at 1.0° west of the dryline (Fig. 12a), temperature profiles in all members are virtually identical with dry-adiabatic lapse rates extending up to near 600 hPa. The dewpoint profiles are more variable than temperature, with QNSE and MYJ slightly moister than the other schemes up to about 800 hPa. As expected in the postdryline environment, all members have zero CAPE and very small values of SRH because the wind profiles are mainly unidirectional. Within the moist sector at 0.5° east of the dryline (Fig. 12b), again, temperature profiles are very similar among the five PBL members with more variability in the dewpoint profiles. Average CAPE values range from 1506 J kg^{-1} in the YSU member to 1948 J kg^{-1} in the QNSE member. MYJ and QNSE have higher CAPE than the other schemes because of a moister dewpoint profile in the lowest ~ 75 hPa. Low variability was present in values of SRH1 and SRH3 with SRH1 ranging from $86 \text{ m}^2 \text{ s}^{-2}$ in YSU to $110 \text{ m}^2 \text{ s}^{-2}$ in MYJ and SRH3 ranging from $190 \text{ m}^2 \text{ s}^{-2}$ in QNSE to $222 \text{ m}^2 \text{ s}^{-2}$ in ACM2. The low variability in SRH is reflected in the similar hodographs at the bottom left of Fig. 12b. At 1.0° , 1.5° , 2.0° , and 2.5° east of the dryline, larger differences among the schemes begin to emerge. At these distances, CAPE values are much higher in MYJ and QNSE than in ACM2, YSU, and MYNN, with the differences most pronounced at 1.5° east of the dryline where CAPE values were just above 2250 J kg^{-1} in MYJ and QNSE, and ranging from about 1500 to 1750 J kg^{-1} in MYNN, YSU, and ACM2. The larger CAPE values in MYJ and QNSE were mainly the result of the moister low-level dewpoint profiles in these members. Additionally, at distances farther east, the temperature profiles begin to exhibit more variability especially centered around the 800-hPa level where the MYJ and QNSE members are noticeably warmer than YSU, ACM2, and MYNN, which is consistent with their tendency to have more

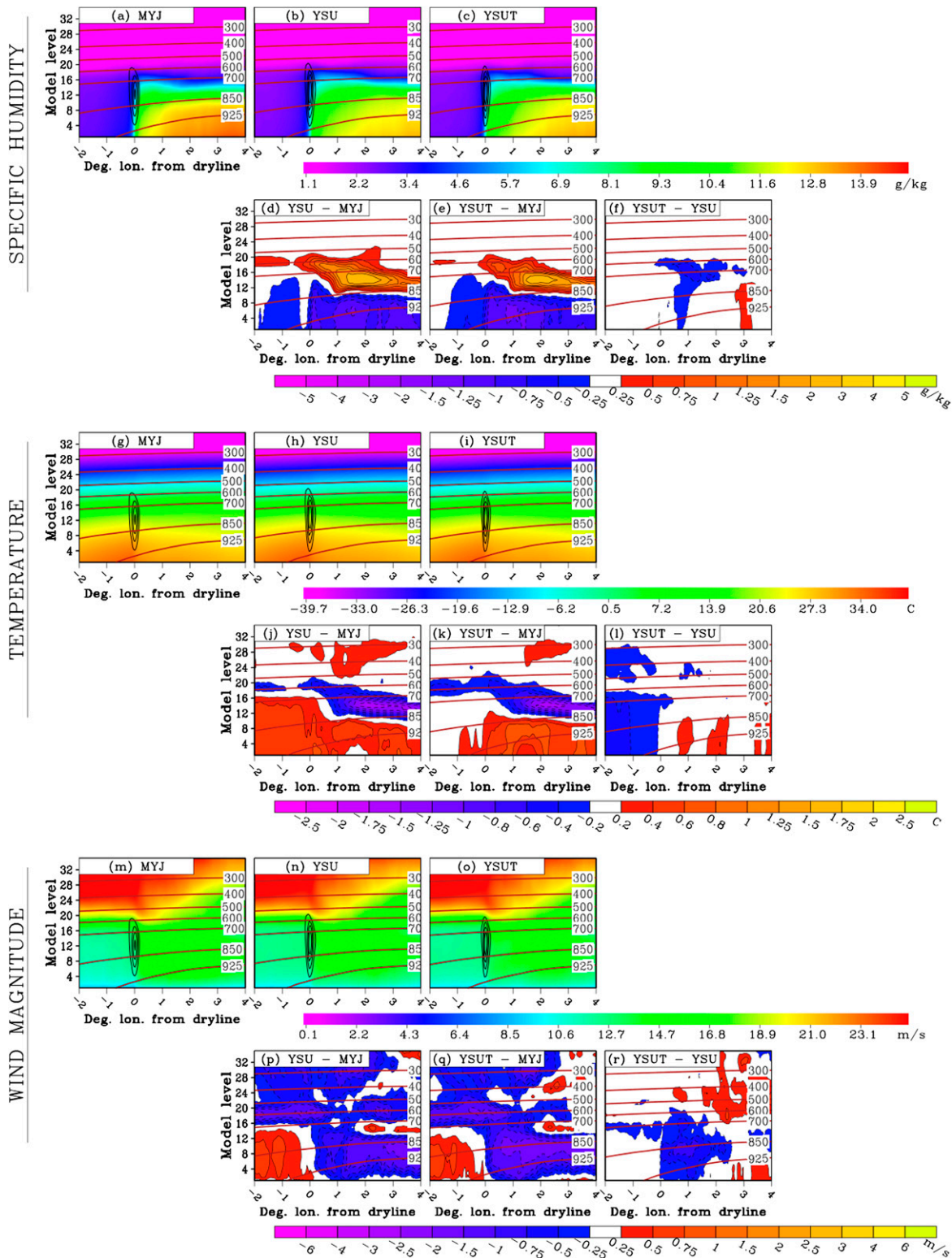


FIG. 11. Composite vertical cross sections of specific humidity (g kg^{-1} ; shaded), pressure (hPa; red contours), and upward vertical velocity (Pa s^{-1} ; black contours at 1 Pa s^{-1} interval from 21 to 26 Pa s^{-1}) over all 2011 cases for (a) MYJ, (b) YSU, and (c) YSU-T. Pressure (hPa; red contours) and specific humidity difference relative to MYJ (g kg^{-1} ; shaded) are given for (d) YSU and (e) YSU-T. (f) Specific humidity difference (g kg^{-1} ; shaded) between YSU and YSU-T. (g)–(l), (m)–(r) As in (a)–(f), but for temperature and wind magnitude, respectively.

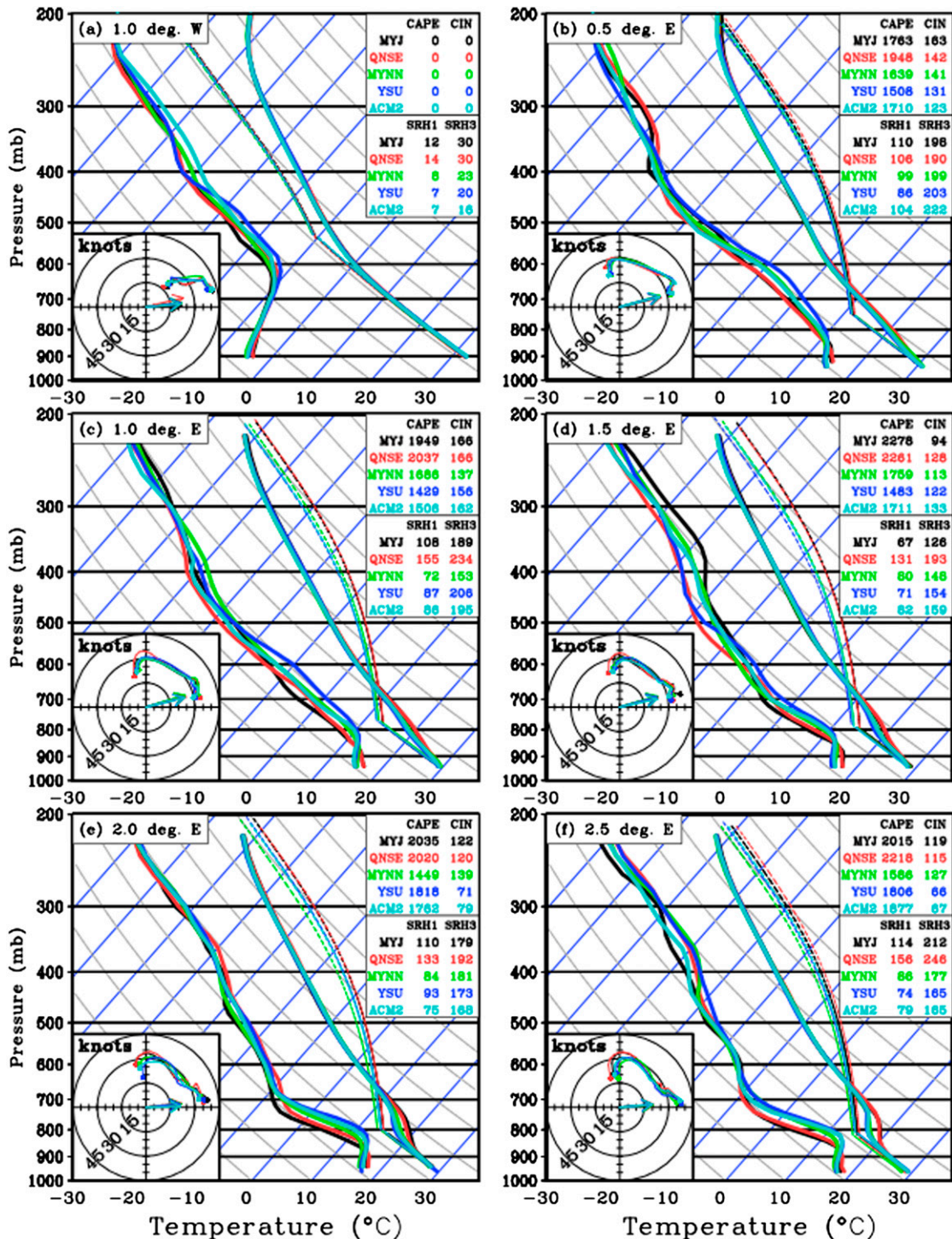


FIG. 12. Dryline-relative composite soundings and hodographs over the lowest 800 hPa of each profile from MYJ, QNSE, MYNN, YSU, and ACM2 for 2011–12 (30 cases). Solid lines depict the temperature and dewpoint traces, and the dashed lines trace the path of surface-based air parcels. The north–south “anchor point” of the composite soundings was found by following the dryline 1° south from its northernmost point. Then, the composites were constructed by taking averages over all cases at the following distances relative to the dryline anchor point: (a) 1.0° west, (b) 0.5° east, (c) 1.0° east, (d) 1.5° east, (e) 2.0° east, and (f) 2.5° east. CAPE, CIN, and SRH over the bottom 100- and 300-hPa layers are shown for each member (at the top right). The text color of each member corresponds to the color of each member’s temperature and dewpoint trace. In the hodographs the storm motion vector is shown, which was computed following [Davies-Jones et al. \(1990\)](#).

pronounced capping inversions. Furthermore, at distances 1.0° east of the dryline and greater, values of SRH exhibit more variability. The faster PBL wind speeds in MYJ, and especially in QNSE (e.g., Figs. 10x– α), result in more “looped” hodographs and higher SRH relative to ACM2, MYNN, and YSU. For example, at 1.0° east of the dryline (Fig. 12c), SRH1 was 108 and $155 \text{ m}^2 \text{ s}^{-2}$ in MYJ and QNSE, respectively, compared to 72, 86, and $87 \text{ m}^2 \text{ s}^{-2}$ in MYNN, ACM2, and YSU, respectively.

Similar to the analysis of the composite vertical cross sections, to evaluate the impact of modifications made to YSU in the YSU-T member, Fig. 13 shows composite soundings for the YSU and YSU-T PBL members for 2011 (14 cases). In general, the temperature profiles at all distances from the dryline are very similar, and the dewpoint profiles exhibit slightly more variability with the main differences being a tendency for slightly more moist dewpoint profiles in lower levels in YSU. Differences in CAPE were less than 150 J kg^{-1} and stronger low-level winds in YSU resulted in much larger values of SRH at 0.5° and 1.0° east of the dryline.

g. Strength of vertical dryline-induced circulation

Several observational and modeling-based studies of the dryline have found that virtual potential temperature gradients across the dryline result in a baroclinic solenoidal circulation pattern (e.g., Parsons et al. 1991; Ziegler and Hane 1993; Ziegler et al. 1995; Hane et al. 1997; Atkins et al. 1998; Ziegler and Rasmussen 1998). Maximum vertical velocities within the upward branch of this circulation have been found to be $\sim 5 \text{ m s}^{-1}$ and it is believed that this circulation is often a major contributor to convective initiation. The model resolution used in this study is sufficient to at least partially resolve this circulation; thus, in this section composite cross sections of the near-dryline vertical wind fields are examined in Fig. 14, which is constructed similarly to the cross sections in Figs. 10 and 11, except the cross sections are zoomed in on the area from 1.0° west to 1.0° east of the dryline. The composites were constructed for 2011 cases, so that all six available PBL schemes could be compared. The pattern in vertical velocity magnitude is similar for all six PBL members. Maximum upward vertical velocities occur between 850 and 700 hPa and are centered directly over the dryline, while maximum downward vertical velocities occur at or just below 400 hPa and are centered slightly east of the dryline. On average, the strongest vertical velocities occur in the YSU and YSU-T members, with maxima in the composites of 55.9 and 55.3 cm s^{-1} , respectively. ACM2 had the smallest maximum vertical velocity at 37.1 cm s^{-1} , while MYJ, QNSE, and MYNN fell in the middle with 46.1 , 46.6 , and 42.5 cm s^{-1} , respectively. Note, the compositing

removes much of the along-dryline variability and the averages are taken over many cases so that strong local maxima are averaged out. However, examining the maximum vertical velocities at various points along the dryline for individual cases, we typically find that the largest upward vertical velocities are in the range of 1.5 – 3.0 m s^{-1} .

4. Summary and discussion

This study examined six versions of the WRF Model that were identically configured except for their scheme to parameterize vertical effects of turbulent mixing. The WRF Model simulations were run by the Center for Analysis and Prediction of Storms in support of NOAA/Hazardous Weather Testbed Spring Forecasting Experiments conducted during 2010–12; covered a CONUS domain with 4-km grid spacing; and used the PBL schemes MYJ, MYNN, QNSE, ACM2, YSU, and YSU-T (a version of YSU that was modified in an effort to alleviate its well-known warm and dry bias by reducing vertical mixing).

Specifically, because of their importance to convective initiation over the southern high plains, as well as their strong dependence on vertical mixing processes in the PBL, this study focuses on 24-h forecast dryline position. Furthermore, the sensitivities of the vertical distribution of thermodynamic and kinematic variables associated with the dryline and near-dryline environment were examined. The main results are summarized below.

For two case studies (12 May 2010 and 24 May 2011), large eastward errors in 24-h forecast dryline position were found. The magnitude of the eastward error was dependent on the PBL scheme and ranged from 0.8° to 2.8° . In both cases, the dryline position errors resulted in large areas being forecast to be outside of the moist sector where there would have been little risk for severe weather, when in reality these areas were within the moist sector where severe weather from dryline-initiated storms occurred. Examining the evolution of the forecast dewpoint from the initialization time in each of the case studies, a dry bias near and west of the dryline could be traced back to the NAM initial conditions. Thus, it was suspected that in these cases, the dry bias in the NAM partially contributed to the dryline errors.

Examining aggregate statistics on forecast dryline position errors, a statistically significant systematic eastward bias was very apparent. Depending on the set of cases and the PBL scheme examined, the mean eastward errors ranged from about 0.5° to 1.25° . Generally, the local schemes MYJ and QNSE had the smallest eastward errors, while the nonlocal schemes (ACM2 and YSU) had the largest eastward errors. However, there were two exceptions to this rule: MYNN, a local scheme, tended to have eastward position errors as large or larger than the

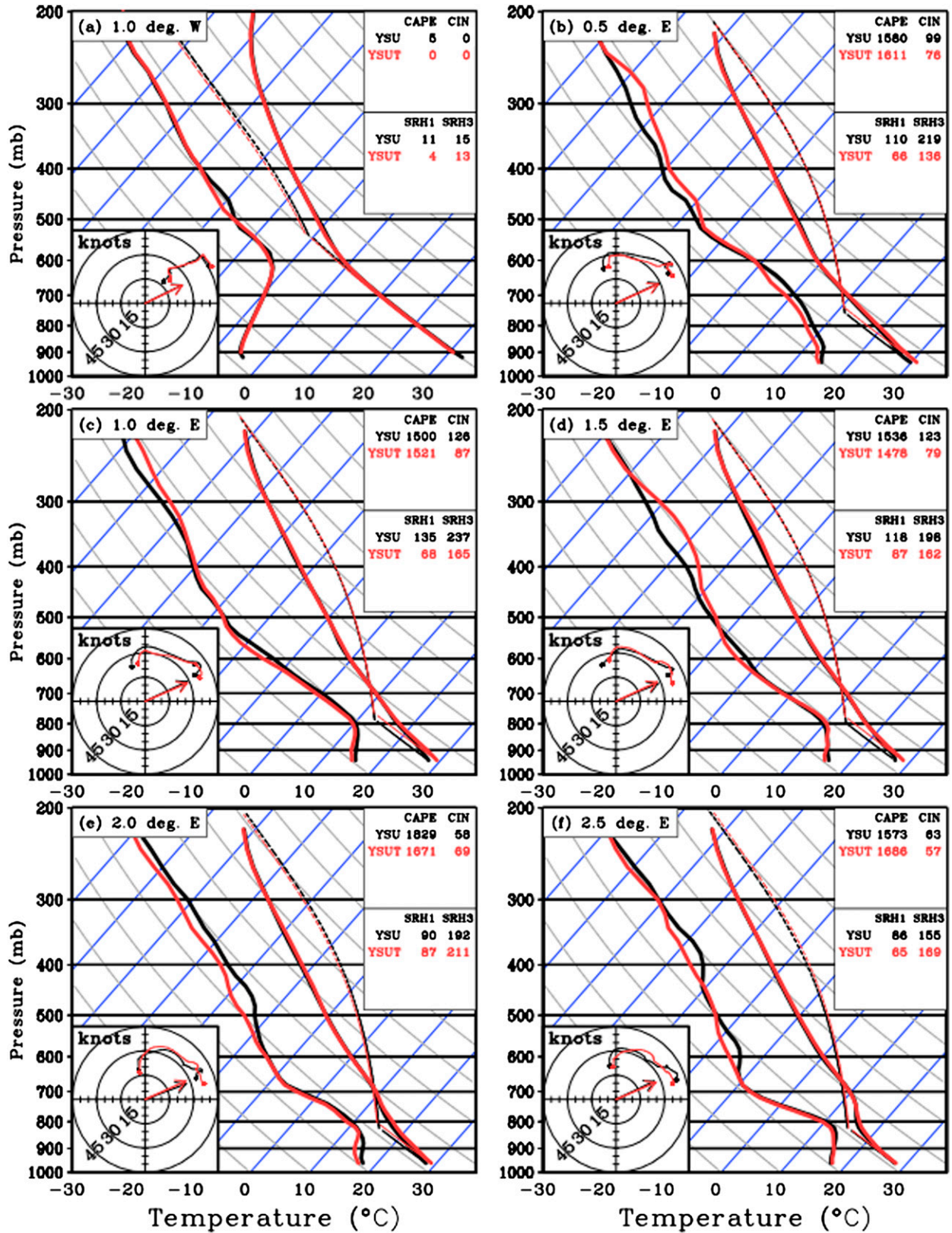


FIG. 13. As in Fig. 12, but for profiles from YSU and YSU-T for the 2011 drylines (14 cases).

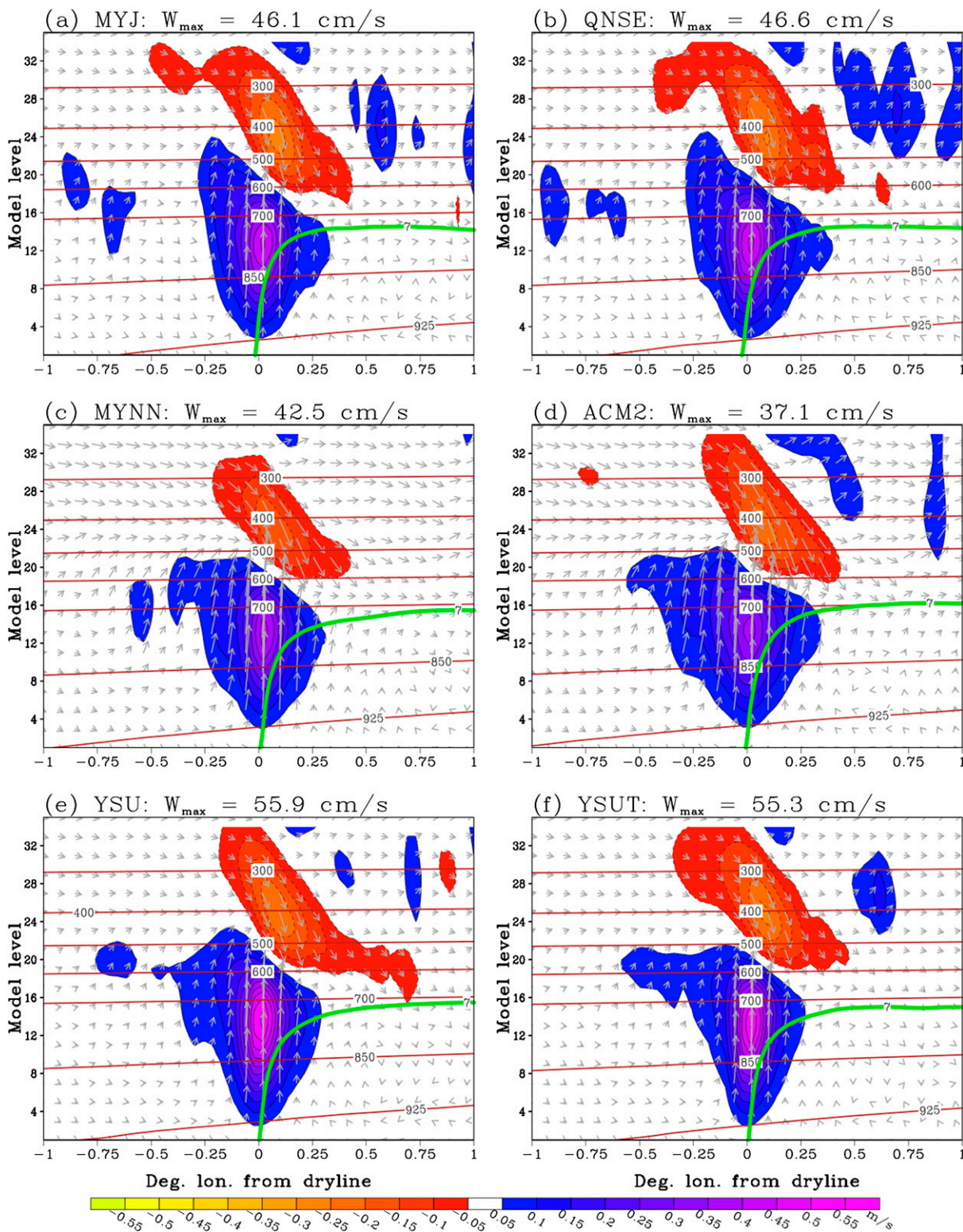


FIG. 14. Dryline-relative composite vertical velocity magnitude (m s^{-1} ; shaded) for 2011 (14 cases). Wind vectors depict the u and w components with the w component multiplied by a factor of 50 to emphasize the vertical component. Pressure (hPa) is shown by the dark red contours. The 7 kg kg^{-1} specific humidity contour (green) is shown to delineate the moist sector. The max vertical velocity in each cross section is provided (at the top). Each displays a different PBL member: (a) MYJ, (b) QNSE, (c) MYNN, (d) ACM2, (e) YSU, and (f) YSU-T.

nonlocal schemes, and YSU-T, a nonlocal scheme that was only run during 2011, had smaller eastward errors than the local schemes (although its dryline positions were not significantly different than MYJ). Examining the relationship between the bias of the 2-m dewpoint from the initial conditions and the 24-h forecast dryline position revealed that these two variables were significantly correlated. Thus, it appeared that a systematic dry bias in the NAM analysis at 0000 UTC near and west of the dryline explained much of the eastward position errors. Examining the 24-h forecast dryline positions separately for each year further supported the influence of the NAM dry bias. During 2010 and 2011, dry biases in the NAM over the region from 29° to 39°N and 105° to 99°W were -2.0° and -1.25°C , respectively, with corresponding large eastward biases in forecast dryline position. However, during 2012, there was almost no bias (0.02°C) in 2-m dewpoint from the NAM, and the corresponding 24-h dryline position errors in the MYJ and QNSE were near zero, while those in the MYNN were about 0.6° east, which was much less than in 2010 and 2011, during which MYNN had eastward errors greater than 1.0° . The reduction in the 2-m dewpoint bias of the NAM ICs was likely related to a major upgrade of the NAM model and data assimilation system that occurred in October 2011. Thus, we believe that dryline position errors in future SSEF system configurations that use the NAM for ICs will have results similar to those of 2012, rather than the earlier years examined.

To gain further insight into how the various PBL schemes depicted the PBL and how they may have been related to the dryline position errors, a procedure was developed to construct dryline-relative composite vertical cross sections of the near-dryline environment for each PBL member. The cross sections of specific humidity revealed that MYNN, ACM2, and YSU had deeper and drier PBLs than MYJ and QNSE and closely matched results presented in [Coniglio et al. \(2013\)](#). In addition, examining the differences in specific humidity with respect to MYJ, a strong dependence was found on the distance from the dryline. For MYNN, ACM2, and YSU, the largest positive moisture differences relative to MYJ were centered between 850 and 700 hPa and occurred between 1.0° and 3.0° east of the dryline. In the temperature composites, the largest negative temperature differences relative to MYJ in the MYNN, ACM2, and YSU members occurred in the 850–700-hPa layer about 2.0° – 3.5° east of the dryline, which reflected a stronger capping inversion in MYJ relative to the other members. Positive temperature differences existed in the layer adjacent to the ground. The temperature results were consistent with an overall deeper and warmer PBL in the MYNN, ACM2, and YSU members relative

to MYJ. The differences in the temperature and moisture cross sections were generally consistent with the differences in forecast dryline position errors; that is, the tendency to produce warmer, drier, and deeper PBLs implies stronger vertical mixing, which results in the dryline mixing farther eastward. Thus, the MYJ and QNSE schemes, which had shallower, moister, and cooler PBLs relative to the other schemes, also had more westward dryline positions, while the ACM2, MYNN, and YSU schemes, which had deeper, drier, and warmer PBLs, had more eastward dryline positions.

The composite vertical cross sections of wind magnitude revealed that ACM, MYNN, and YSU generally had stronger wind speeds in the PBL east of the dryline relative to MYJ, which is likely the result of more vertical mixing in these schemes relative to MYJ. Also, in the QNSE scheme, wind speeds were generally faster than MYJ in the PBL east of the dryline.

In comparisons of composite vertical cross sections between YSU and YSU-T, only very small differences in temperature, moisture, and wind were found. This was somewhat surprising given the relatively large differences in forecast dryline position in the YSU and YSU-T members. Further investigation beyond the scope of this study is needed to resolve this apparent discrepancy.

To complement the composite vertical cross sections, composite soundings at various distances to the east and west of the dryline were presented to provide perspective on how sensitive products relevant to severe weather forecasting are to the PBL schemes. The main findings from the composite sounding analyses were that the largest differences between the schemes occurred at 1.0° , 1.5° , 2.0° , and 2.5° east of the dryline. At these distances, CAPE values were much higher in MYJ and QNSE than ACM2, YSU, and MYNN, which was mainly the result of moister low-level dewpoint profiles in these members. Also, at these distances, the temperature profiles in the MYJ and QNSE members were noticeably warmer than YSU, ACM2, and MYNN, reflecting their more pronounced capping inversions. Furthermore, at 1.0° east of the dryline and greater, SRH exhibited more variability, with the faster PBL wind speeds in MYJ, and especially QNSE, resulting in more “looped” hodographs and higher SRHs than ACM2, MYNN, and YSU. In the comparisons of YSU and YSU-T, the most notable differences were with SRHs at 0.5° and 1.0° east of the dryline where stronger low-level winds in YSU resulted in much larger values of SRH.

Finally, to examine the depiction of the dryline-induced vertical circulation, composite cross sections of the near-dryline vertical wind fields were examined for each PBL member. The patterns in vertical velocity among all six PBL members were very similar.

Maximum upward velocities occurred between 850 and 700 hPa and were centered directly over the dryline, while maximum downward velocities occurred at or just below 400 hPa and were centered slightly east of the dryline. YSU and YSU-T had the strongest upward velocities, and ACM2 had the smallest.

The results of this study illustrate how important it is in convection-allowing modeling applications to consider more than just the depiction of the environmental temperature and moisture. Coniglio et al. (2013) made this point after finding favorable results for MYNN comparing observed versus forecast sounding structures in preconvective environments and noted, “The fact that MYNN performed best [...] does not necessarily mean it will perform the best when evaluated for explicit forecasts of convection or for other characteristics of the simulations that depend on turbulent mixing (e.g., the position of drylines and fronts).” Because current convection-allowing modeling systems like the HRRR utilize MYNN, further work should be conducted to improve its depiction of forecast dryline position. Furthermore, the nonlocal scheme YSU-T should be examined in more detail because of its superior performance in forecast dryline position.

Acknowledgments. Funding was provided by NOAA/Office of Oceanic and Atmospheric Research under NOAA–University of Oklahoma Cooperative Agreement NA11OAR4320072, U.S. Department of Commerce. CAPS SSEF forecasts were supported by the NOAA Collaborative Science, Technology, and Applied Research (CSTAR) Program with supplementary support from NSF Grant AGS-0802888. MX was supported by NSF Grants OCI-0905040, AGS-0941491, AGS-1046171, and AGS-1046081. CAPS forecasts were supported by an allocation of advanced computing resources provided by the National Science Foundation. The computations were performed on Athena (a Cray XT4) at the National Institute for Computational Science (<http://www.nics.tennessee.edu/>). CAPS utilized resources from the OU Supercomputing Center for Research and Education for ensemble postprocessing. We thank two anonymous reviewers for many helpful comments/suggestions that improved the manuscript.

REFERENCES

- Alexander, C. R., and Coauthors, 2013: High-Resolution Rapid Refresh (HRRR) model and production advancements for 2013 with targeted improvements for reliable convective weather guidance in the National Airspace System. *Proc. 16th Conf. on Aviation, Range, and Aerospace Meteorology (ARAM)*, Austin, TX, Amer. Meteor. Soc., 9.2. [Available online at <https://ams.confex.com/ams/93Annual/webprogram/Paper218637.html>.]
- Atkins, N. T., R. M. Wakimoto, and C. L. Ziegler, 1998: Observations of the finescale structure of a dryline during VORTEX 95. *Mon. Wea. Rev.*, **126**, 525–550, doi:10.1175/1520-0493(1998)126<0525:OOTFSO>2.0.CO;2.
- Benjamin, S. G., and Coauthors, 2004a: An hourly assimilation–forecast cycle: The RUC. *Mon. Wea. Rev.*, **132**, 495–518, doi:10.1175/1520-0493(2004)132<0495:AHACTR>2.0.CO;2.
- , G. A. Grell, J. M. Brown, T. G. Smirnova, and R. Bleck, 2004b: Mesoscale weather prediction with the RUC hybrid isentropic–terrain-following coordinate model. *Mon. Wea. Rev.*, **132**, 473–494, doi:10.1175/1520-0493(2004)132<0473:MWPWTR>2.0.CO;2.
- Brown, J., and Coauthors, 2012: Rapid Refresh replaces the Rapid Update Cycle at NCEP. *2012 Canadian Meteorological and Oceanographic Society Congress/21st Conf. on Numerical Weather Prediction/25th Conf. on Weather and Forecasting*, Montreal, QC, Canada, CMOS, 3B1.
- Chen, F., and J. Dudhia, 2001: Coupling an advanced land-surface–hydrology model with the Penn State–NCAR MM5 modeling system. Part I: Model description and implementation. *Mon. Wea. Rev.*, **129**, 569–585, doi:10.1175/1520-0493(2001)129<0569:CAALSH>2.0.CO;2.
- Chou, M.-D., and M. J. Suarez, 1994: An efficient thermal infrared radiation parameterization for use in general circulation models. NASA Tech. Memo. 104606, Vol. 3, 85 pp.
- Clark, A. J., and Coauthors, 2012: An overview of the 2010 Hazardous Weather Testbed Experimental Forecast Program Spring Experiment. *Bull. Amer. Meteor. Soc.*, **93**, 55–74, doi:10.1175/BAMS-D-11-00040.1.
- Coffer, B. E., L. C. Maudlin, P. G. Veals, and A. J. Clark, 2013: Dryline position errors in experimental convection-allowing NSSL-WRF Model forecasts and the operational NAM. *Wea. Forecasting*, **28**, 746–761, doi:10.1175/WAF-D-12-00092.1.
- Coniglio, M. C., 2012: Verification of RUC 0–1-h forecasts and SPC mesoscale analyses using VORTEX2 soundings. *Wea. Forecasting*, **27**, 667–683, doi:10.1175/WAF-D-11-00096.1.
- , J. Correia, P. T. Marsh, and F. Kong, 2013: Verification of convection-allowing WRF Model forecasts of the planetary boundary layer using sounding observations. *Wea. Forecasting*, **28**, 842–862, doi:10.1175/WAF-D-12-00103.1.
- Davies-Jones, R., D. Burgess, and M. Foster, 1990: Test of helicity as a tornado forecast parameter. Preprints, *16th Conf. on Severe Local Storms*, Kananaskis Park, AB, Canada, Amer. Meteor. Soc., 588–592.
- Du, J., J. McQueen, G. DiMego, Z. Toth, D. Jovic, B. Zhou, and H.-Y. Chuang, 2006: New dimension of NCEP Short-Range Ensemble Forecasting (SREF) system: Inclusion of WRF members. *WMO Expert Team Meeting on Ensemble Prediction Systems*, Exeter, United Kingdom, WMO. [Available online at http://www.emc.ncep.noaa.gov/mmb/SREF/WMO06_full.pdf.]
- Fujita, T. T., 1958: Structure and movement of a dry front. *Bull. Amer. Meteor. Soc.*, **39**, 574–582.
- Gao, J., M. Xue, K. Brewster, and K. K. Droegemeier, 2004: A three-dimensional variational data analysis method with recursive filter for Doppler radars. *J. Atmos. Oceanic Technol.*, **21**, 457–469, doi:10.1175/1520-0426(2004)021<0457:ATVDAM>2.0.CO;2.
- Hane, C. E., H. B. Bluestein, T. M. Crawford, M. E. Baldwin, and R. M. Rabin, 1997: Severe thunderstorm development in relation to along-dryline variability: A case study. *Mon. Wea. Rev.*, **125**, 231–251, doi:10.1175/1520-0493(1997)125<0231:STDIRT>2.0.CO;2.
- Hu, M., M. Xue, and K. Brewster, 2006: 3DVAR and cloud analysis with WSR-88D level-II data for the prediction of Fort Worth

- tornadic thunderstorms. Part I: Cloud analysis and its impact. *Mon. Wea. Rev.*, **134**, 675–698, doi:10.1175/MWR3092.1.
- Hu, X.-M., J. W. Nielsen-Gammon, and F. Zhang, 2010: Evaluation of three planetary boundary layer schemes in the WRF Model. *J. Appl. Meteor. Climatol.*, **49**, 1831–1843, doi:10.1175/2010JAMC2432.1.
- Janjić, Z. I., 2002: Nonsingular implementation of the Mellor–Yamada level 2.5 scheme in the NCEP Meso model. NCEP Office Note No. 437, NOAA/NWS, 61 pp. [Available online at <http://www.emc.ncep.noaa.gov/officenotes/newernotes/on437.pdf>.]
- Kong, F., and Coauthors, 2010: Evaluation of CAPS multi-model Storm-Scale Ensemble Forecast for the NOAA HWT 2010 Spring Experiment. *25th Conf. Severe Local Storms*, Amer. Meteor. Soc., Paper P4.18. [Available online at https://ams.confex.com/ams/91Annual/webprogram/Manuscript/Paper181680/Kong_24thWF20thNWP-extendedAbstract.pdf.]
- , and Coauthors, 2011: CAPS Storm-Scale Ensemble Forecast in HWT 2011 Spring Experiment: Sensitivity of WRF physics on QPF. *Extended Abstracts, 12th Users' Workshop*, Boulder, CO, NCAR. [Available online at http://www2.mmm.ucar.edu/wrf/users/workshops/WS2011/Power%20Points%202011/6_3_Kong_WRFworkshop_11.pdf.]
- Marshall, C. H., K. C. Crawford, K. E. Mitchell, and D. J. Stensrud, 2003: The impact of the land surface physics in the operational NCEP Eta Model on simulating the diurnal cycle: Evaluation and testing using Oklahoma Mesonet data. *Wea. Forecasting*, **18**, 748–768, doi:10.1175/1520-0434(2003)018<0748:TOTLS>2.0.CO;2.
- Mellor, G. L., and T. Yamada, 1982: Development of a turbulence closure model for geophysical fluid problems. *Rev. Geophys.*, **20**, 851–875, doi:10.1029/RG020i004p00851.
- Miller, P. A., M. F. Barth, and L. A. Benjamin, 2005: An update on MADIS observation ingest, integration, quality control and distribution capabilities. Preprints, *21st Int. Conf. on Interactive Information and Processing Systems*, San Diego, CA, Amer. Meteor. Soc., J7.12. [Available online at <https://ams.confex.com/ams/pdfpapers/86703.pdf>.]
- , —, —, R. S. Artz, and W. R. Pendergrass, 2007: MADIS support for UrbaNet. Preprints, *14th Symp. on Meteorological Observation and Instrumentation/16th Conf. on Applied Climatology*, San Antonio, TX, Amer. Meteor. Soc., JP2.5. [Available online at <http://ams.confex.com/ams/pdfpapers/119116.pdf>.]
- Mlawer, E. J., S. J. Taubman, P. D. Brown, M. J. Iacono, and S. A. Clough, 1997: Radiative transfer for inhomogeneous atmosphere: RRTM, a validated correlated- k model for the long-wave. *J. Geophys. Res.*, **102**, 16 663–16 682, doi:10.1029/97JD00237.
- Nakanishi, M., 2000: Large-eddy simulation of radiation fog. *Bound.-Layer Meteor.*, **94**, 461–493, doi:10.1023/A:1002490423389.
- , 2001: Improvement of the Mellor–Yamada turbulence closure model based on large-eddy simulation data. *Bound.-Layer Meteor.*, **99**, 349–378, doi:10.1023/A:1018915827400.
- , and H. Niino, 2004: An improved Mellor–Yamada level-3 model with condensation physics: Its design and verification. *Bound.-Layer Meteor.*, **112**, 1–31, doi:10.1023/B:BOUN.0000020164.04146.98.
- , and —, 2006: An improved Mellor–Yamada level-3 model: Its numerical stability and application to a regional prediction of advection fog. *Bound.-Layer Meteor.*, **119**, 397–407, doi:10.1007/s10546-005-9030-8.
- Noh, Y., W. G. Cheon, S.-Y. Hong, and S. Raasch, 2003: Improvement of the K -profile model for the planetary boundary layer based on large eddy simulation data. *Bound.-Layer Meteor.*, **107**, 401–427, doi:10.1023/A:1022146015946.
- Parsons, D. B., M. A. Shapiro, R. M. Hardesty, R. J. Zamora, and J. M. Intrieri, 1991: The finescale structure of a west Texas dryline. *Mon. Wea. Rev.*, **119**, 1242–1258, doi:10.1175/1520-0493(1991)119<1242:TFSOAW>2.0.CO;2.
- Plein, J. E., 2007: A combined local and nonlocal closure model for the atmospheric boundary layer. Part I: Model description and testing. *J. Appl. Meteor. Climatol.*, **46**, 1383–1395, doi:10.1175/JAM2539.1.
- R Development Core Team, cited 2013: R: A language and environment for statistical computing. R Foundation for Statistical Computing, Vienna, Austria. [Available online at <http://www.R-project.org>.]
- Rhea, J. O., 1966: A study of thunderstorm formation along dry lines. *J. Appl. Meteor.*, **5**, 59–63.
- Roebber, P. J., D. M. Schultz, B. A. Colle, and D. J. Stensrud, 2004: Toward improved prediction: High-resolution and ensemble modeling systems in operations. *Wea. Forecasting*, **19**, 936–949, doi:10.1175/1520-0434(2004)019<0936:TIPHAE>2.0.CO;2.
- Rogers, E., and Coauthors, 2009: The NCEP North American Mesoscale modeling system: Recent changes and future plans. Preprints, *23rd Conf. on Weather Analysis and Forecasting/19th Conf. on Numerical Weather Prediction*, Omaha, NE, Amer. Meteor. Soc., 2A.4. [Available online at <https://ams.confex.com/ams/pdfpapers/154114.pdf>.]
- Schaefer, J. T., 1986: The dryline. *Mesoscale Meteorology and Forecasting*, P. S. Ray, Ed., Amer. Meteor. Soc., 549–572.
- Skamarock, W. C., and Coauthors, 2008: A description of the Advanced Research WRF version 2, NCAR Tech Note, NCAR/TN-475+STR, 113 pp. [Available online at http://www.mmm.ucar.edu/wrf/users/docs/arw_v3.pdf.]
- Sukoriansky, S., B. Galperin, and V. Perov, 2005: Application of a new spectral theory of stable stratified turbulence to the atmospheric boundary layer over sea ice. *Bound.-Layer Meteor.*, **117**, 231–257, doi:10.1007/s10546-004-6848-4.
- Thompson, G., R. M. Rasmussen, and K. Manning, 2004: Explicit forecasts of winter precipitation using an improved bulk microphysics scheme. Part I: Description and sensitivity analysis. *Mon. Wea. Rev.*, **132**, 519–542, doi:10.1175/1520-0493(2004)132<0519:EFOWPU>2.0.CO;2.
- Xue, M., D. Wang, J. Gao, K. Brewster, and K. K. Droegemeier, 2003: The Advanced Regional Prediction System (ARPS), storm-scale numerical weather prediction and data assimilation. *Meteor. Atmos. Phys.*, **82**, 139–170, doi:10.1007/s00703-001-0595-6.
- , and Coauthors, 2010: CAPS realtime storm scale ensemble and high-resolution forecasts for the NOAA Hazardous Weather Testbed 2010 Spring Experiment. *25th Conf. on Severe Local Storms*, Denver, CO, Amer. Meteor. Soc., 7B.3. [Available online at <https://ams.confex.com/ams/pdfpapers/176056.pdf>.]
- Ziegler, C. L., and C. E. Hane, 1993: An observational study of the dryline. *Mon. Wea. Rev.*, **121**, 1134–1151, doi:10.1175/1520-0493(1993)121<1134:AOSOTD>2.0.CO;2.
- , and E. N. Rasmussen, 1998: The initiation of moist convection at the dryline: Forecasting issues from a case study perspective. *Wea. Forecasting*, **13**, 1106–1131, doi:10.1175/1520-0434(1998)013<1106:TJOMCA>2.0.CO;2.
- , W. J. Martin, R. A. Pielke, and R. L. Walko, 1995: A modeling study of the dryline. *J. Atmos. Sci.*, **52**, 263–285, doi:10.1175/1520-0469(1995)052<0263:AMSOTD>2.0.CO;2.